FLORIDA STATE UNIVERSITY

COLLEGE OF ARTS AND SCIENCES

SEARCH FOR LEPTOPHILIC HIGGS BOSON DECAYS TO LONG-LIVED SCALAR PARTICLES WITH REGIONS OF INTEREST (ROIS) AND MACHINE LEARNING IN CMS

By

SUHO KIM

A Dissertation submitted to the
Department of Physics
in partial fulfillment of the
requirements for the degree of
Doctor of Philosophy

2022

Suho Kim defended this dissertation on Nov 18, 2022.
The members of the supervisory committee were:

Ted Kolberg
Professor Directing Disseration

Elizabeth Hammock
University Representative

Todd Adams
Committee Member

Kohsaku Tobioka
Committee Member

Peter Hoeflich
Committee Member

The Graduate School has verified and approved the above-named committee members, and certifies that the dissertation has been approved in accordance with university requirements.

To my parents, who always suspected I'd end up here

ACKNOWLEDGMENTS

Thanks to many people.

TABLE OF CONTENTS

LIST OF TABLES

LIST OF FIGURES

ABSTRACT

We present a search for long-lived particles (LLPs) produced in gluon fusion Higgs production mode (ggH), using a novel strategy of Regions of Interest (ROIs). Regions of Interest are collections of pair-wise track vertices fitted by the vertex fitter in CMSSW. The analysis focuses LLPs with lifetimes that result in decays in the tracker region, with concentration on the ggH production mode for the highest Higgs cross-section. Variables of the constructed ROIs become inputs for our Deep Neural Network (DNN) Machine Learning (ML) algorithms, as a main discriminator between the signal and the background. We focus on the Standard Model (SM) τ lepton final state. This final state is particulary interesting, given τ lepton final state exclusion limits are mostly omitted in precedent analyses, due to τ leptons' non trivial reconstruction mechanisms in CMS. In order to trigger on the ggH production mode of the Higgs particle, decaying into its leptonic signature via exotic long-lived scalar particles, we exploit the B-parking trigger. B-parking trigger is newly installed High Level Trigger path in the CMS detector, targetting soft displaced muon. The trigger was installed in 2018, totalling in integrated Luminosity value of 41fb^{-1}. No excess of events over the standard model expectation is observed. The results are interpreted in the context of exotic Higgs decays to a pair of long-lived scalars (S). We set limits on the branching ratio of the Higgs to LLPs, $\mathbf{B}$(H$\rightarrow SS \rightarrow \tau\tau\tau\tau$) , as a function of the proper lifetime. The analysis has strongest discriminant power for the scalar particle's lifetime from 1mm to 10mm for 7and 15GeV, and from 10mm to 100mm for 40 and 55GeV. The analysis' exclusion limit on the branching ratio for τ lepton final state ($\mathbf{B}$(H$\rightarrow SS \rightarrow \tau\tau\tau\tau$)) is one of the most stringent results from the LHC detectors. The 9% at 10mm for 7GeV, 5% at 10mm for 15 GeV, 9% at 100mm for 40 GeV, and 20% at 1000mm for 55 GeV are respective values.

CHAPTER 1

INTRODUCTION

The discovery of particles at the electroweak scale, such as the top quark at Fermilab's CDF and D0 [1, 2] and the Higgs boson at the Large Hadron Collider (LHC) in CERN [3, 4], led to discovery of all constituents in the Standard Model (SM). The SM describes the nature of fundamental particles and their interactions with precision. In spite of its success, the SM suffers from the few obstacles: the evidence of neutrino masses and mixing [5], the obsevations of bullet clusters confirming the presence of dark matter (DM) [6, 7, 8, 9, 10], and baryon-antibaryon asymmetry [11] all remain unexplained in the framework of SM. In addition, the SM suffers from the naturalness problem. To solve such issues, one needs to look for physics Beyond the Standard Model (BSM).

To search for the BSM, the high energy physics (HEP) community has completed many researches both in theoretical and experimental sides. Theoretical high energy physics community approached the issue with 2 main approaches. The first approach tackles the issue of precision. Although the SM is very well constrained model, further precision of particles in the SM, especially those in the electroweak scale, gives new insight for the BSM physics. For instance, the CDF collaboration recently discovered a 7σ deviation of the W boson mass from the SM prediction [12]. The W boson mass deviation has been interpreted for new physics using the framework of the Standard Model Effective Field Theory (SMEFT) [13]. In SMEFT, the SM operators from the SM Lagrangian are used to build 5,6,8-dimensional new terms for the Lagrangian. The SMEFT scalar, fermion, or vector extension gives hint for new insight for the BSM and its phenomenology [13]. The other approach aims to build an entirely new Lagrangian term, which can be appended to the current SM Lagrangian term. The BSM Lagrangian introduces new particle fields and should address unsolved issues in the current SM framework. The new particles' mass scale can range from those in the collider level upto the astrophysical level.

To find the new BSM particles, the experimental high energy physics community conducted many different researches based on both collider and astrophysical data. Experimental physicists invested strenuous effort on data from the collider physics, since lightest particles from popular theory, such as supersymmetry (SUSY), were within the collider's hard scattering energy level. Experimentalists searching for the BSM particles can also divide their main approaches into 2, the first with prompt decay of the BSM particle and the second with long-lived lifetime signature. CMS analysis targeting the BSM particles with prompt lifetime have been fully studied and resulted in no deviation from the SM prediction [14]. However, the second approach, which has not been fully investigated, is when particles decay with Long-Lived signature, in other words, Long-Lived particles (LLP). This signature is uniquely interesting and challenging for scientists. It requires different analysis strategy depending on the mass scale (MS) and lifetime ($c\tau$) of the BSM particle. Thus, this frontier has been perceived as the blue ocean for HEP experimentalists, to the extent that a new detector solely targeting LLPs is planned to be built [15].

In this dissertation, we focus on the LLPs originating from the LHC, specifically the CMS, review precedent analyses, and propose a novel strategy. Searches for LLPs decaying into final states containing jets were investigated at the Tevatron ($\sqrt{s}$ = 1.96 TeV) by both CDF [16] and D0 [17] Collaborations, at the LHC by the ATLAS and LHCb Collaborations at $\sqrt{s}$ = 7 TeV [18, 19], by the ATLAS, CMS and LHCb Collaborations at $\sqrt{s}$ = 8 TeV [20, 21, 22, 23, 24, 25, 26]. More recently, by the CMS [27, 28, 29, 30, 31, 32] and ATLAS Collaborations [33, 34, 35, 36, 37, 38, 39, 40, 41, 42, 43, 44] at $\sqrt{s}$ = 13 TeV.

CMS Collaboration released a new result in 2021. In the new paper, the Higgs decaying into LLPs, is created in association with a Z vector boson [45]. This analysis' feynman diagram is displayed in figure 1.1. The new analysis shed light on LLPs with lighter masses thanks to the clean dilepton trigger from the associated Z vector boson. Although exclusion limit on branching ratio of the Higgs to the LLPs to b and d-quark were set below unitarity for analyses above, exclusion limit for τ final state has been omitted or presented with values above 1.

However, the Leptophilic model for Twin Higgs and other Higgs models are also highly motivated [46]. Continuous neglect of τ final state limit is not only a poor practice, but overlooks an important unexplored phase space. This analysis searches for LLPs, originating from the Higgs Portal model with the Higgs' Leptophilic nature. Since the coupling strength of the Higgs' to SM fermions are quantified by the Yukawa couplings, focus on Leptophilic Higgs translates into focuses on τ final state decaying back from the LLPs via the Higgs Portal. The 55 GeV maximum scalar mass is set to investigate only on-shell neutral scalar particles from the Higgs. A minimum 7 GeV mass for scalar particles is required to create on-shell τ-lepton pairs. Feynman diagram of the scalar particle production mechanism is depicted in Figure 1.2. Main challenge and reason for omission of a τ lepton analysis is on the different decay modes of τ leptons. τ leptons decay hadronically and leptonically, with several different sub-decay modes. Its decay mode pie chart and CMS detection

Figure 1.1: Feynman diagram of ZH signal process studied in the most recent CMS analysis paper (2021)

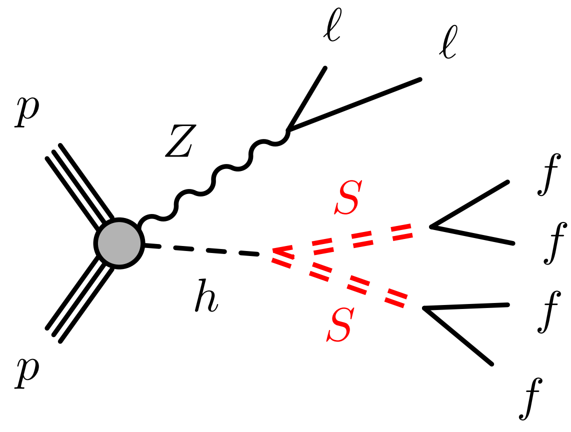

category pie chart are displayed in figures of 1.3 and 1.4 respectively. Developing analysis strategies to optimize the search for each sub-decay modes is extremely complicated, a main reason for the omission or no good exclusion limit in precedent LHC results. To be inclusive of all τ leptons' decay modes, a displaced vertex search can be more efficient than a displaced objects (jet, muon, electrons) search. We exploit the newly developed Regions of Interest mechanism in the tracker volume. Regions of Interest (ROI) form displaced vertex candidates, by fittng pair-wise tracks of Lost-tracks and PackedPFCandidates classes in MINIAOD data into a vertex. ROIs save all relevant track and fitted vertex qualities along with isolation information. These variables are used as input for Machine Learning (ML) algorithms, enabling a highly generic and data-scientific search method.

Figure 1.2: The analysis' signal process feynman diagram. The Higgs is created in gg production mode. The LLP scalar decays into τ lepton.

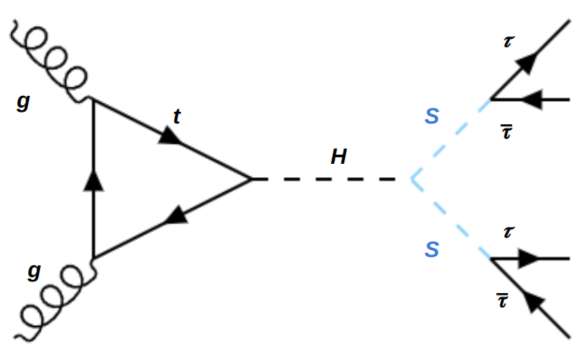

Figure 1.3: τ lepton's decay mode pie chart

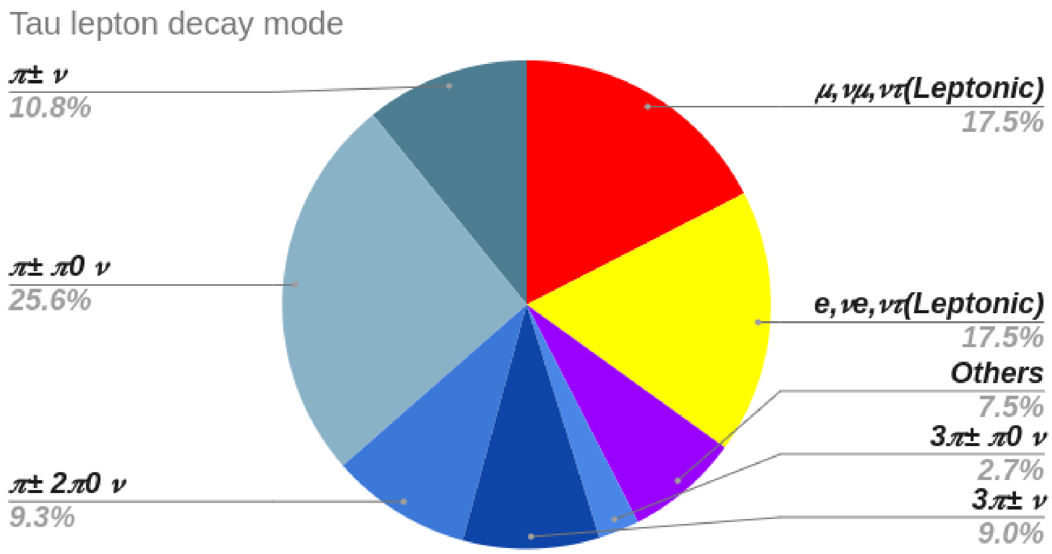

Figure 1.4: τ lepton's detection mode pie chart. Prong means a charged track reconstructed in the tracker volume of the CMS. It corresponds to $\pi^{\pm}$

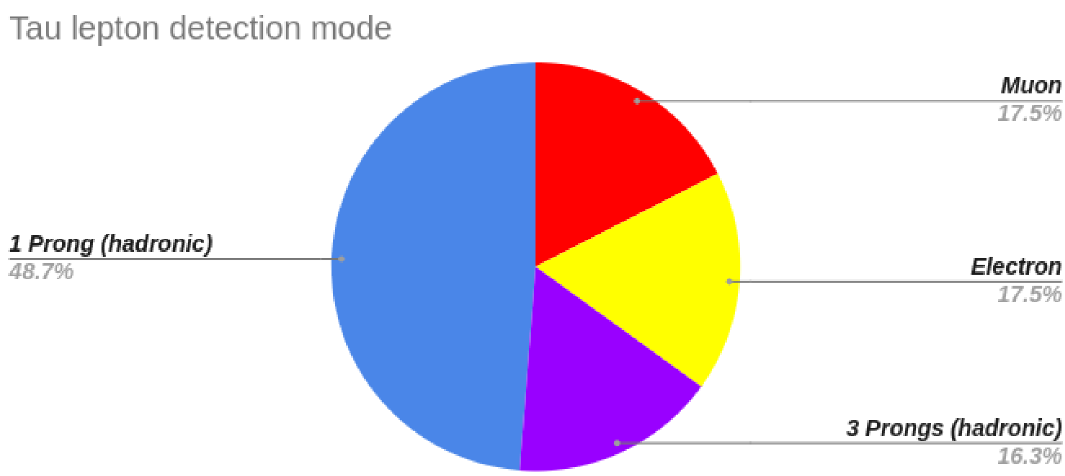

Another challenge is that CMS searches are not optimal for detecting Higgs boson decays due to the soft p_T nature of its decays products. Higgs produced in association with Z vector boson analysis [45] overcame this barrier with help of dilepton trigger. Although ggH production mode gives the largest Higgs crosssection, it complicates the trigger strategy even further. This analysis exploits the τ lepton's leptonic decay, in which the τ lepton decays into a soft muon, using a trigger of B Parking High Level Trigger (HLT) Path implemented in CMS for the 2018 portion of Run 2.

The rest of the dissertation is organized as follows. In Section 2, we discuss the theoretical background of the BSM and LLPs in more details. In Section 3, the CMS detector is thoroughly discussed with emphasis on the tracks and the calorimeter, which are relevant detector parts for the analysis. We discuss how the analysis exploited the b-parking trigger in Section 4, with description of its original motive for the trigger's installation. The physics objects and formation of Regions of Interest are described in Section 5. The machine learning algorithms are futher explained in Section 6. The event selections are presented in Section 7. Section 8 describes the data driven background estimation method. Section 9 describes the background estimation method's validation process and systematic uncertainties. Finally, Section 10 presents the results of the search. We conclude with Section 11.

CHAPTER 2

THE STANDARD MODEL AND ITS FUTURE

In Section 1, we introduced the few obstacles facing the SM: Existance of darkmatter, baryon-antibaryon asymmetry, and the evidence of neutrino masses and mixing. The SM Lagrangian, writted as in formula 2.1, does not have particles' fields which can explain those phenomena.

$$\mathcal{L}_{SM} = \mathcal{L}_{Higgs} + \mathcal{L}_{Gauge} + \mathcal{L}_{Kinetic} + \mathcal{L}_{Yukawa} \tag{2.1}$$

Since it can not be explained by any of the particles' fields in the SM, it requires addition of new particles' fields or new terms in the current SM Lagrangian expression. New terms in the SM Lagrangian entails in new vertices in the Feynman diagram, which open the door for a new understanding of the high energy physics. However, if those observations did not exist, the SM is all complete within its own framework only except for the naturalness problem.

The naturalness problem originates from the fact that the SM Higgs is a scalar particle. The formula 2.1 has three different kinds of fields: boson, fermion, and scalar. Quantum Field Theory (QFT), the humanity's mathematical framework used for the SM, explains matter as an excited state of fermion fields, derived from the canonical quantization of the SM Lagrangian's fermion fields. The fermions' fields have chrial symmetry as demostrated in the kinetic term of the SM Lagrangian in formula 2.2 and 2.3.

$$\mathcal{L}_{L_{kin}} = \bar{L} * i\gamma^{\mu} D_{\mu} L + h.c. \tag{2.2}$$

$$\mathcal{L}_{R_{kin}} = \bar{u} * i\gamma^{\mu} D_{\mu} u + \bar{d} * i\gamma^{\mu} D_{\mu} d + h.c. \tag{2.3}$$

, where dirac matrices are summed up over Lorentz indices for Lorentz invariance, lefthand fermion is a doublet for weak force interaction, and right-hand fermion is a singlet separated by the uptype fermion (neutrinos for leptons) and downtype fermion (electrically charged leptons for leptons). Since fermions with left-hand chriality behaves in a different manner from fermions with right-hand chirality, the covariant derivatives are also different for left-hand kinetic term and right-hand kinetic terms, being defined in 8.2 and in 2.5.

$$D_\mu = i\partial_\mu - \frac{1}{2}g\tau * W_\mu - \frac{1}{2}g^{'}YB_\mu \tag{2.4}$$

$$D_\mu = i\partial_\mu - \frac{1}{2}g^{'}YB_\mu \tag{2.5}$$

, where τ is isospin for SU(2) weak force, and g,W are couplings and fields for the weak theory. g' and B are respective variables for quantum electrodynamics (QED). In equations above, we can see the fermions with lefthand chirality are separated from the righthand chirality.

Likewise, the bosons' fields also satify special symmetries in the QFT framework. The boson satisfy the U(1), SU(2) or SU(3) gauge symmetry, and are expressed in gauge terms as in formula 2.6.

$$\mathcal{L}_{Gauge} = -\frac{1}{4}B_{\mu\nu} * B^{\mu\nu} - \frac{1}{4}W^{\tau}_{\mu\nu} * W^{\mu\nu}_{\tau} - \frac{1}{4}G^{\alpha}_{\mu\nu} * G^{\mu\nu}_{\alpha}. \tag{2.6}$$

,where B,W,G are QED, weak, quantum chromodynamics (QCD) fields, τ, α are SU(2),SU(3) group indices respectively.

These symmetries provice 1 major advantage in QFT, the renormalization. QFT understands the observed mass of particles in terms of its bare mass and correction as in 2.7.

$$m_f^2 = m_{f,0}^2 + \delta m_f^2. \tag{2.7}$$

The chrial and gauge symmetries make correction to be zero, and protect fermion and boson fields from the radiative correction in the renormalization process.

Unlike fermions or gauge bosons, the scalar field of the Higgs boson is not protected by any symmetry and is subject to large radiative corrections, especially from the top quark loop. Thus, for the SM to be valid up to the Planck or Grand Unification Theory (GUT) scales of 10^{16} GeV, the necessary radiative corrections are enormous. One needs an exorbitant amount of fine-tuning to fit the Higgs mass at the observed value of 125GeV. One of the most popular solutions to this problem is Supersymmetry (SUSY), which assigns chirality to the Higgs particle. SUSY solves the fine-tuning problem, neutrino masses, and provides a candidate for DM.

Unfortunately, the LHC has found no significant excess over the SM background in their search for SUSY[14]. Although the non-observation of supersymmetric partner particles does not invalidate SUSY, it makes less attractive among the particle physics community. Non-observation of superpartners, particularly the stop (scalar partner of the top quark) has pushed its mass beyond

1TeV. This generates "little hierarchy" problem, but an alternative solution of "neutral naturalness" remains.

In the framework of neutral naturalness, the top partners are not charged under the SM color group. Because of being colorless, their production crosssection is much smaller, and the present limits on the top partner particles are well below 1TeV. Examples of neutral naturalness models are the Twin Higgs [47], Folded SUSY [48], and the Quirky Little Higgs [49] models. Theoretical models provide the possibility of neutral Long-Lived Particles (LLPs), which may be produced in the proton-proton collisions of the LHC, and decay back to SM particles far from the interaction point (IP).[50] If the mirror QCD gluons form scalar glueballs, the SM Higgs boson can become a "Higgs Portal" between the SM and BSM mirror QCD scalar glueballs. In the Mirror SM and Twin SM models, only the SM Higgs boson can interact with both SM QCD and mirror QCD particles as in figure 2.1. BSM mirror QCD scalar glueballs can only decay back to SM particles via Higgs

Figure 2.1: A cartoon display of Higgs Portal process

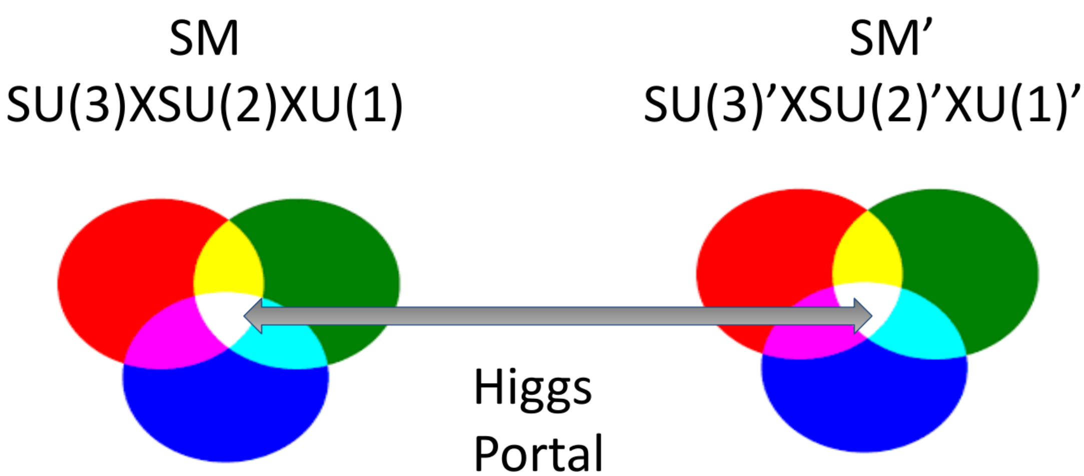

boson decay as well.

Because of its decay as an offshell Higgs boson, its crosssection is highly suppressed. Decay branching ratio to highest mass fermions will be highest following the Yukawa couplings. Decay ratio into b quarks or τ leptons are highest depending on the mirror scalar's mass. However, if the Higgs has leptophilic behavior, decay ratio into τ leptons are always the highest. The displaced decays of the scalars would lead to exotic signatures in the CMS, such as distant innermost tracker hit, displaced vertices, and displaced jets. Phenomenology of long-lived particles in LHC entailed increase in interest of neutral naturalness framework among the particle physics community. [51, 52]. The long-lived scalar model is shown in the Figure 2.2.

Figure 2.2: A diagram display of Higgs Portal process

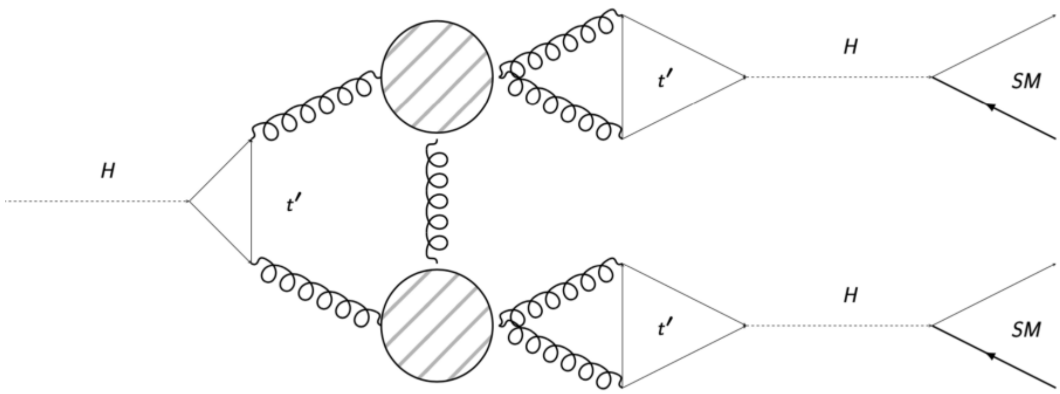

CHAPTER 3

THE CMS DETECTOR

Since the discovery of the neutron in 30s, humanity's aspiration to understand the most fundamental constituents and laws of the physics have only accelerated. Discovery of pions, Kaons, and other hadrons from the cosmic rays in 40s, 50s led to understanding of substructure of those particles with Eightfole way of Gell-Mann. Deep inelastic scattering performed in 60s by the Stanford Linear Accelerator Center (SLAC) confirmed existence of "partons" or "quarks", substructure of those particles. Observance of J-psi and Upsilon mesons in SLAC and MIT put the third generation fermions in the collection of particles. Gargamelle bubble chamber in CERN succeeded in detection of muon neutrinos, postulated by Pauli in 30s from the beta decay experiment. CERN's UA1 and UA2 in 80s confirmed existence of first particles in the electroweak scale, namely the W and Z bosons. Fermilab's CDF and D0 in 90s confirmed existence of the top quark, the heaviest particle in the SM. All these discoveries of the most fundamental particles of the universe happened within a half-century. As much as we appreciate the predecessor physicists for the phenomenal analytic and statistical works, we need to appreciate the evolution of the experimental apparatus as well. Although simple design of bubble chamber or detection of cosmic rays is still a helpful insight for particle physics research, physicists wanted to create the cosmic and very early phase of the universe on our terra. Progress from the linear accelerator to TeV scale circular high energy accelerator was achieved by physicists, engineers, and others. Its pinnacle came with construction fo the LHC, situated in CERN, the home of UA(1-5).

3.1 The LHC and the CMS

The LHC is the world's largest and highest energy particle collider. The LHC was built for a decade from 1998 to 2008. The construction was completed in collaboration with 100 countries and 10000 scientists around the globe, demostrating the ethos of global cooperation of the physics community and its majestic scale. The LHC construction, which costed 5 billion us dollars for its construction , costs 5.5 billion dollars per year for its electric and computing power consumption [53]. The LHC is built in a tunnel 328 feet underground at CERN, on the Franco-Swiss border near Annecy, France and Geneva, Switzerland. The LHC shoots bunches of protons and lead ions near the speed of light, enabled by the 27 km ring of superconducting magnets with a number of accelerating apparati. One can infer the LHC name's origin, given that it's 27km long, shoots hadrons of protons, and collide them each other at 0.9997 fraction of the speed of light.

CERN is an acclerator complex, which includes succession of machines with increasingly higher energies. Each machine accelerates a beam of particles to a threshold of desired energy, and injects

Figure 3.1: Picture of the CERN complex [54]

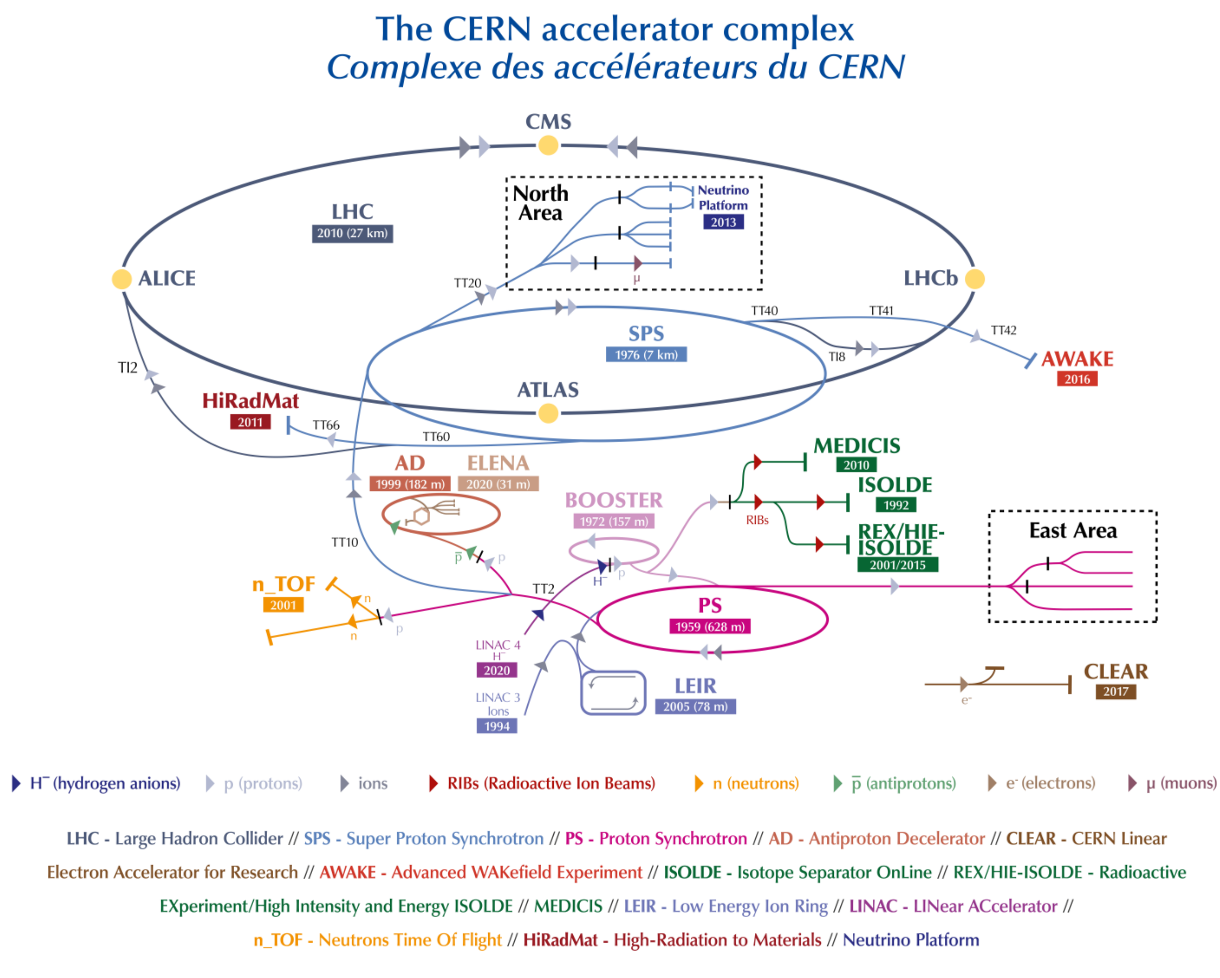

the beam into the next machine in the chain. The next machine brings the beam to an even higher energy and repeats the cycle until the entering the LHC. The LHC is the last element of this chain, in which the beams reach their highest energies. The LHC is cooled to 1.9K and maintained at ultrahigh vacuum status.

The goal of LHC was to discover the last remaining piece of the SM, the Higgs boson. The LHC already succeeded in its primary goal, with discovery of the Higgs boson bo the CMS and ATLAS in July 4th, 2012. However, the LHC's goal does not stop there. As mentioned in 2, there still exists several unanswered questions in high energy physics. LHC wants to address them. It wants to discover the SUSY particles, dark matters, and other exotic particles to help us better understand the most fundamental nature of the universe.

In order to tackle these issues more efficienctly, there are 4 main detectors in the LHC: Compact Muon Solenoid (CMS), A Toroidal LHC Apparatus (ATLAS), A Large Ion Collider Experiment (ALICE), and LHCb. CMS and ATLAS are general purpose colliders. They were used for the discovery of the Higgs Boson in 2012. They are used for an entire range of the high energy physics, investigating the SUSY particles to dark matter to precision QCD to Lepton Universality. ALICE is a lead-lead collider, targeting to study a phase of matter called the Quark-Gluon Plasma (QGP). Study of QGP helps us better understand quarks and gluons behavior when they esacape the confinement of the QCD. Similar research is done in Brookhaven National Laboratory's Pioneering High Energy Nuclear Interaction eXperiment (BNL's PHENIX). LHCb is a b-factory. It wants to test or challenge "Lepton Universality", claiming that interaction between leptons and a gauge boson measures the same for each lepton. Similar research is done in BaBar of SLAC and BelleII of KoEnerugi Kasokuki kenkyu kiko (KEK). The analysis of this dissertation entirely derives from data obtained in the CMS. Following subsections detail parts and functions of each part of the CMS.

The CMS consists of 5 main parts: the tracker, the electromagnectic calorimeter (ECAL), the hadronic calorimeter, the superconducting magnet and the Muon chamber. We will review each part's hardware information and its role in terms of the entire CMS. The order of review is identical as a particle's trajectory from the beamspot as in 3.4, except that the tracker is placed at the end for its connection to my analysis' trigger strategy.

3.1.1 Calorimetry

ECAL of the CMS. Electron and photon energies are measured in the ECAL with high precision. CMS has a compact scintillating crystal calorimeter with excellent performance for energy resolution. The ECAL consists of 75,000 lead-tungstate (PbWO4) crystals with coverage in pseudorapidity upto 3.0. As photons and electrons shower through the crystals, their radiation light is detected by silicon avalanche photodiodes (APDs) in the barrel and vacuum phototriodes

Figure 3.2: Picture of the CMS viewed from the beam direction [55]

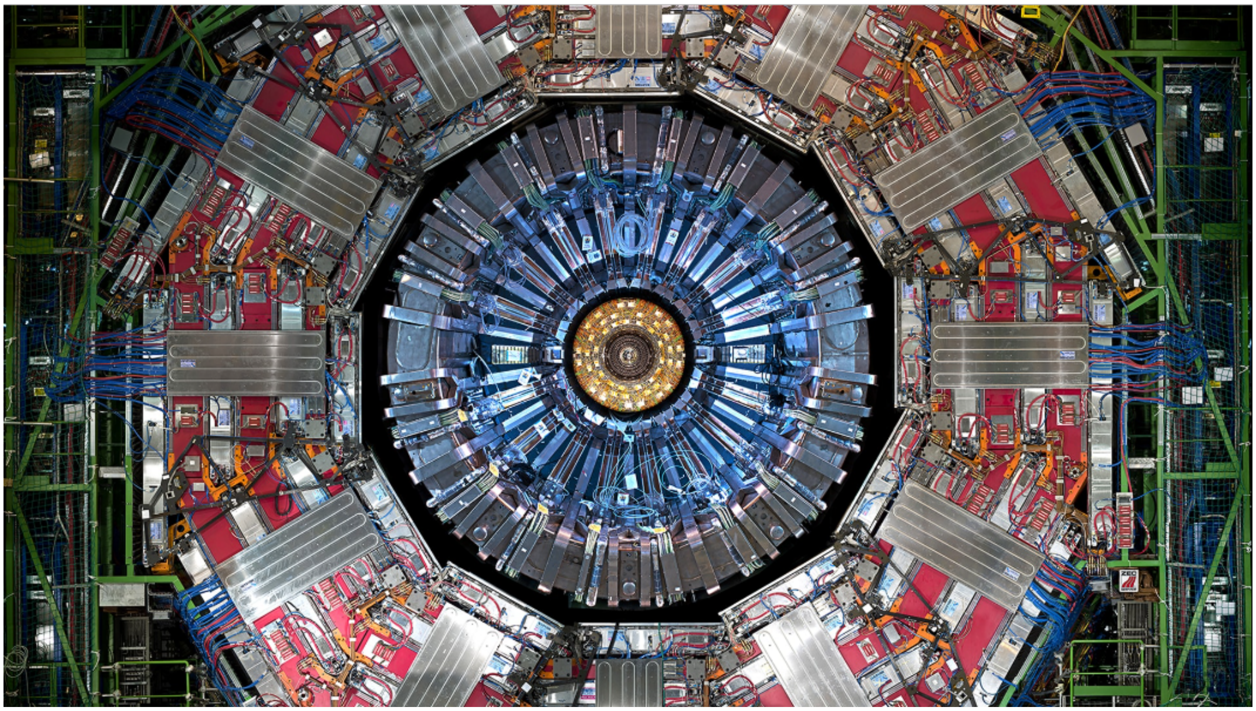

(VPTs) in the endcap. ECAL distinguises photons from electron based on the the energy dispersion on the iη-iϕ map as photon's energy is deposited into a wider area. ECAL can also distinguish π^0, which decay into 2 photons, from photons originating from the hard scattering. ECAL's preshower system installed in the front of the endcap is used for π^0 rejection and the detection of photons.

HCAL of the CMS. The ECAL is surrounded by brass/scintillator sampling Hadron Calorimeter (HCAL) with pseudorapidity upto 3.0. Strongly interacting SM particles, such as quarks, gluons, deposit their energy into the HCAL. These particles are in form on hadrons, due to color confinement of QCD, and hadrons' shower is more messy than electromagnetically interacting particles. We indentify these strongly interacting particles, as a jet, which is a narrow cone of hadrons and other particles produced by the hadronization of a quark or gluon. HCAL plays an important role in the identification and measurement of neutrinos by measuring the energy and direction of jets. Since the initial momentum in the transverse plane, which is a plane perpendicular to the beam(z) direction, is 0, the final transeverse momentum is also equal to 0. If the final transverse momentum is not equal to 0, or there is missing transverse energy (MET), it means there is an undetected particle leaving the collider in the opposite direction, signaling the identification of neutrinos. However, it could also be interpreted as a signature of a BSM particle based on other information. Thus,

Figure 3.3: Cartoon of the CMS with its subpart annotated [56]

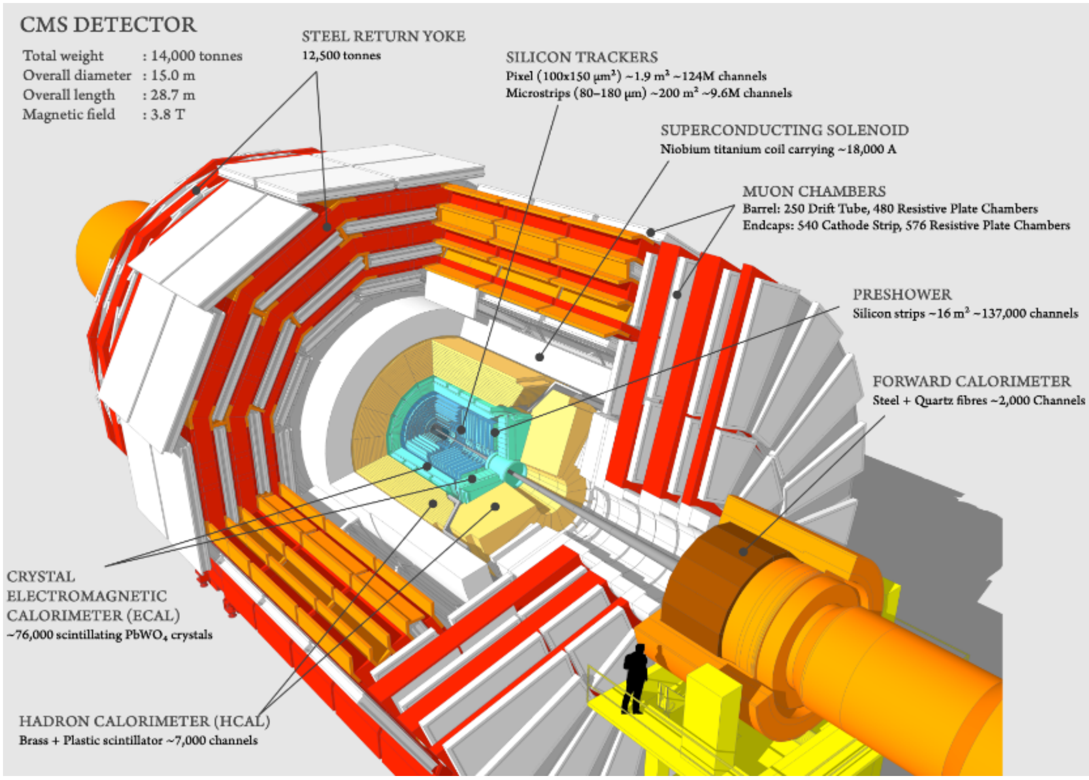

Figure 3.4: Cross-section of the CMS detector as a particle traverses through the apparatus [56]

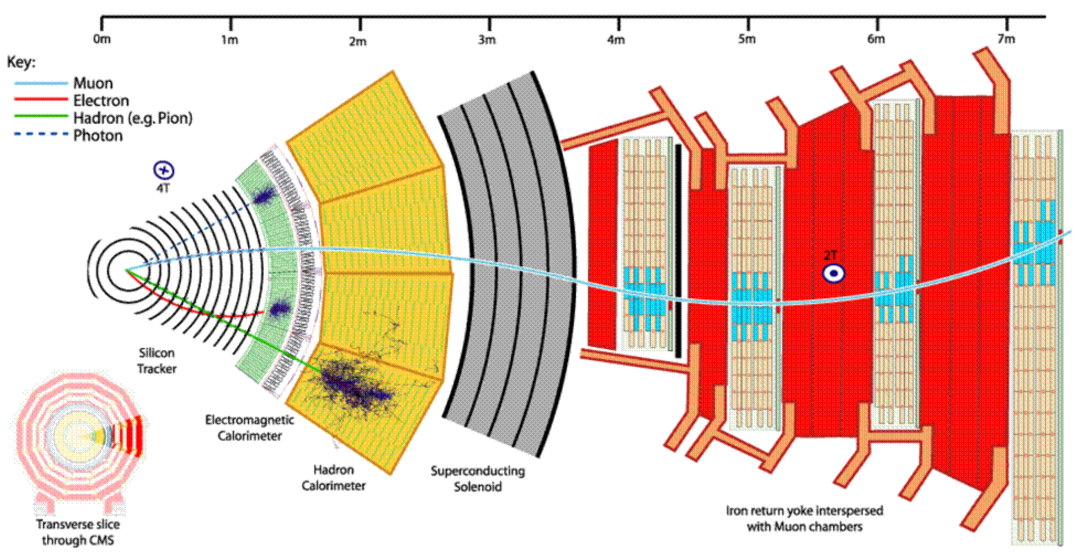

Figure 3.5: Schematic view of the ECAL. [57]

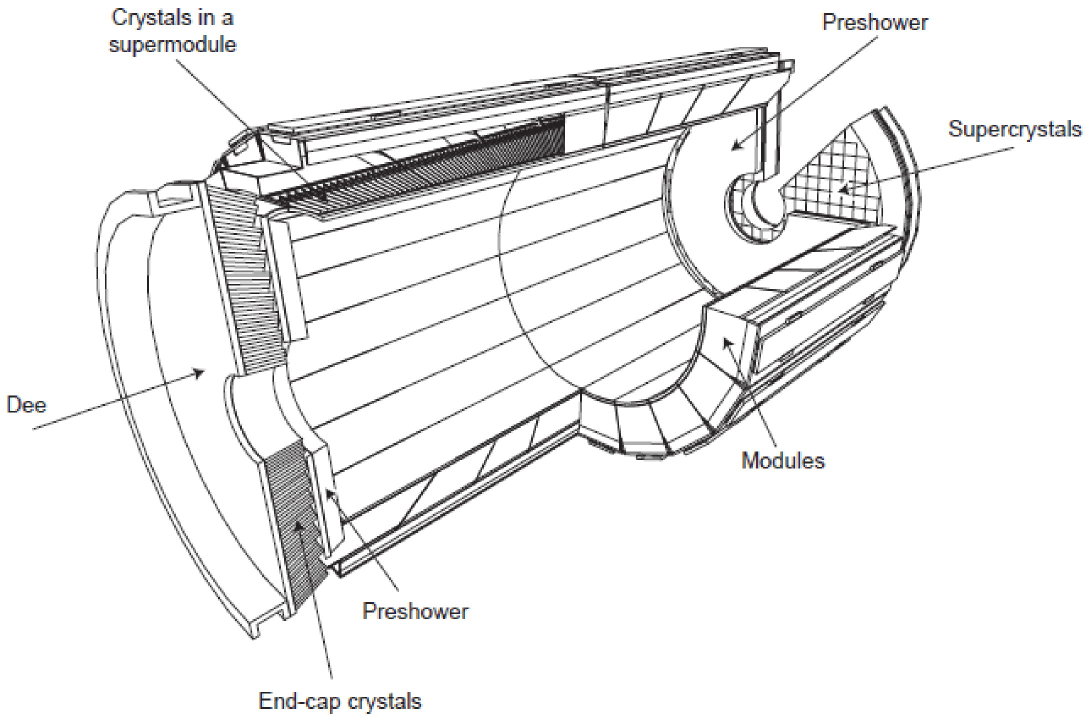

Figure 3.6: Cross-section of the HCAL in the CMS detector. It shows the Barrel, endcap, front, and outside portion. [58]

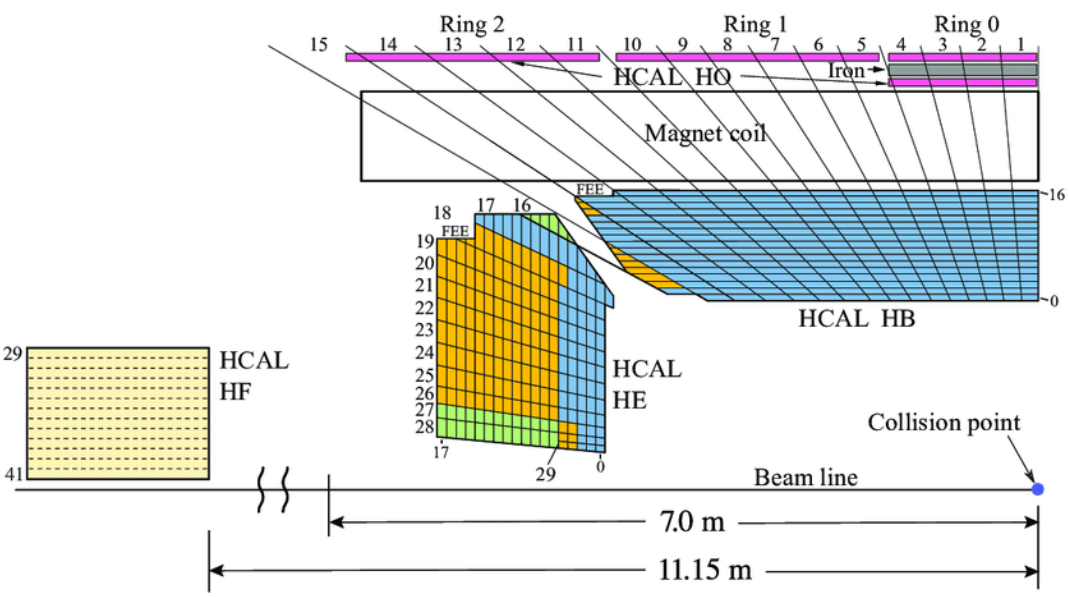

MET plays a crucial role for finding new BSM particles, like the supersymmetric partners of quarks and gluons. In addition, precise measurement of high energy jets is important for searches for high mass Standard Model and SMEFT study.

Since HCAL plays such a crucial role in detection of new physics, the structure of HCAL is also highly complex. The scintillation light, converted by wavelength-shifting (WLS) fibers inside the scintillator tiles, is conneted to photodetectors. This light is detected by hybrid photodiodes(HPDs) that can operate in high axial magnetic fields. While most of the HCAL's Barrel (HB) and endcap (HE) are positioned inside the CMS magnet, HCAL outside and front (HO,HF) are located outside the magnet to detect particles from high energy showers. The HB and HE are sampling calorimeters with 50 mm thick copper absorber plates interleaved with 4 mm thick scintillator sheets. The HCAL's Barrel (HB) is complemented by a "tail-catcher" to ensure that hadronic showers are sampled with nearly 11 hadronic interaction lengths to contain high energy jets. HF installed at each end of the CMS detector which provide coverage up to a pseudorapidity of 5.0, with steel absorber plates used for the harsher radiation environment of the forward systems. The HF ensure full geometric coverage for the measurement of the transverse energy in the event. HCAL's comprehensive geometrical coverage and precise energy measurements are crucial for BSM searches in Vector-Boson Fusion (VBF) Higgs production mode, where high energetic jets decay back-to-back at high pseudorapidity.

Muons and tau leptons deposit only a very small fraction of their energy in the calorimeters, and are identified with tracking and muon detector subsystems' information in reconstruction level.

3.1.2 The superconducting Magnet of the CMS

The superconducting magnet encompasses the inner tracker and the calorimetry, while outside of the superconducting magnet is the flux return system and muon detector. The superconducting magnet is 13m-long, 5.9 m inner diameter, 12 kilo-ton, 4 T, the core part of the CMS. The CMS magnet system consists of a superconducting coil, the magnet yoke (barrel and endcap), a vacuum tank and ancillaries such as cryogenics, power supplies and process controls.

Magnetic field provided by the superconducting magnet is essential for the momentum measurement of charged particles Electrically charged particles' trajectories are bent inside the magnetic field due to the Lorentz force. The particles leave their trajectories in the tracker, and the trajectory is used to calculate momentum of each particle. The 4T magnetic field also enables detection of isolated electrons produced by the decays of b,W,Z particles. CMS ECAL uses these electrons to be calibrated to an accuracy of a fraction of a percent. The magnetic flux is returned via a 1.5 m thick saturated iron yoke interleved in four stations of Muon Chamber.

3.1.3 The Muon Chamber of the CMS

Figure 3.7: Cross-section of the Muon Chamer in the CMS detector. It shows the 4 layers of the drift tube (DT) cross-section viewed from the z-axis. [55]

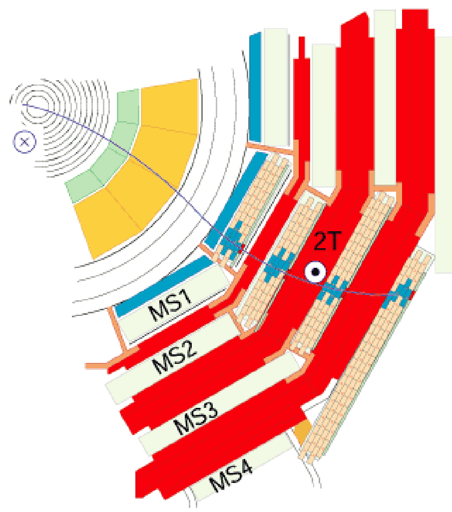

Muons, which is considered to be stable in the CMS perspective due to its lifetime, provide clean signatures unlike hadrons. Muon system's reconstruction efficiency is better than 98% over the full pseudorapidity range. Each muon station has several layers of aluminum drift tubes (DT) for the barrel region and cathode strip chambers (CSCs) for the endcap region. The DT and CSC detectors are used to obtain a precise measurement of the 4 vector of the muons. The DT and CSC are complemented by resistive plate chambers (RPCs), which are fast gaseous muon detectors that provide a muon trigger system. Large thickness of the absorber material (iron) ensures muons do not escape the detector, thereby increasing its identification efficiencys.

Muons detected and triggered by the Muon Chamber feeds into muon reconstruction algorithms. In reconstruction algorithms, position, direction vectors and an estimate of the muon transverse momentum are used as seeds for the track fits using the Kalman filter technique. The result is a collection of reco::track objects, reconstructed as "standalone muons". For each standalone muon track, a search for tracks matching it among those reconstructed in the inner tracking system ("inner tracks" or "silicon tracks") is performed. The best-matching tracker track and "standalone muon" pair, based on the Kalman filter technique, gives a collection of reco::Track objects referred to as "global muons". A complementary approach, by considering all tracker tracks to be potential muon candidates with compatible signatures in the calorimeters and in the muon system, provides a collection of reco::Track objects referred to as "tracker muons".

3.2 Tracker of the CMS more in detail

Figure 3.8: Cross-section of the trackers in the CMS detector. It shows the pixels in the inner tracker for more precise vertexing and the silicon strips on the outer trackers. Silicon strips are tilted with respect to previous layers of strips. [59]

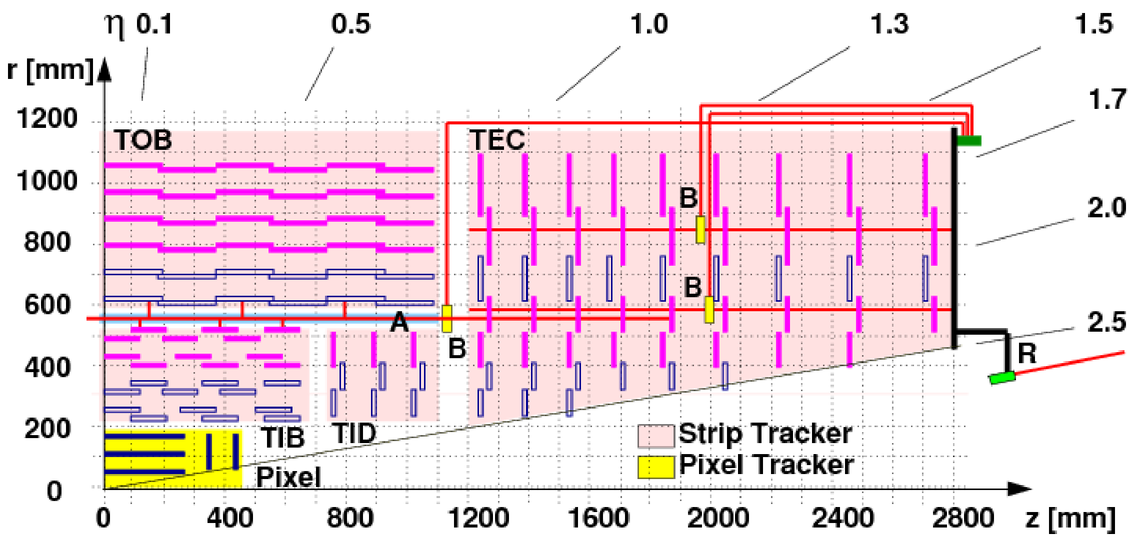

The inner tracker is the first detector material sitting around the LHC beampipe. It consists of the pixel cells in the innermost part, and silicon strip sensors in the outer part of the tracker. The inner-most tracking material consists of 3 layers of silicon pixel detectors. During Run 2 of 2017-2018, additional pixel layer was added for even better performance. The square pixel detectors with high granularity are extremely radiation resistant and provide most accurate position information. The outer layers of the tracker consist of strip sensors, which are more financially affordable. They are of 5.8 m length, 2.6m diameter, 10 layers, and consists of 25,000 silicon strip sensors in cylindrical shape. The system provides analogue data from about 10 million channels. Each layer is oriented a slight off-angle with respect to the previous layer for 2D position measurement.

The CMS tracking system, with the magnetic field coming from the superconducting magnet, reconstruct muons, electrons and charged hadrons' tracks with high momentum resolution with efficiency better than 98% in pseudorapidity upto 2.5. They provide the required granularity and precision to deal with high track multiplicities. For muons, with information from the measurements of the muon chamber, the tracking system contributes to even better resolution.

The tracker is quintessential for many physics analyses. Its closest placement to the interaction point provides precise vertex reconstruction and measurement of the impact parameter (IP) of tracks. The trackers' reconstruction for secondary vertices is critical for b-tagging, a method of detecting jets arising from b quark decays. It is a frequently used tool in many CMS groups. For instance, physicists studying Lepton Universality uses b-tagging, enabled by the tracker's good vertex reconstruction efficiency, to identify physics process involving B mesons to Kaons. In addition, physicists use b-tagging to identify top quarks, which is another good portal for BSM physics along with the Higgs boson and mostly decay into b-jets. The tracker's impact parameter values also play significant role in discovery of BSM physics targetting for LLPs. LLPs IP values are starkly different from SM particles' IP values.

3.3 Trigger of the CMS

Figure 3.9: Cross-section of the trackers in the CMS detector. It shows the pixels in the inner tracker for more precise vertexing and the silicon strips on the outer trackers. Silicon strips are tilted with respect to previous layers of strips. [59]

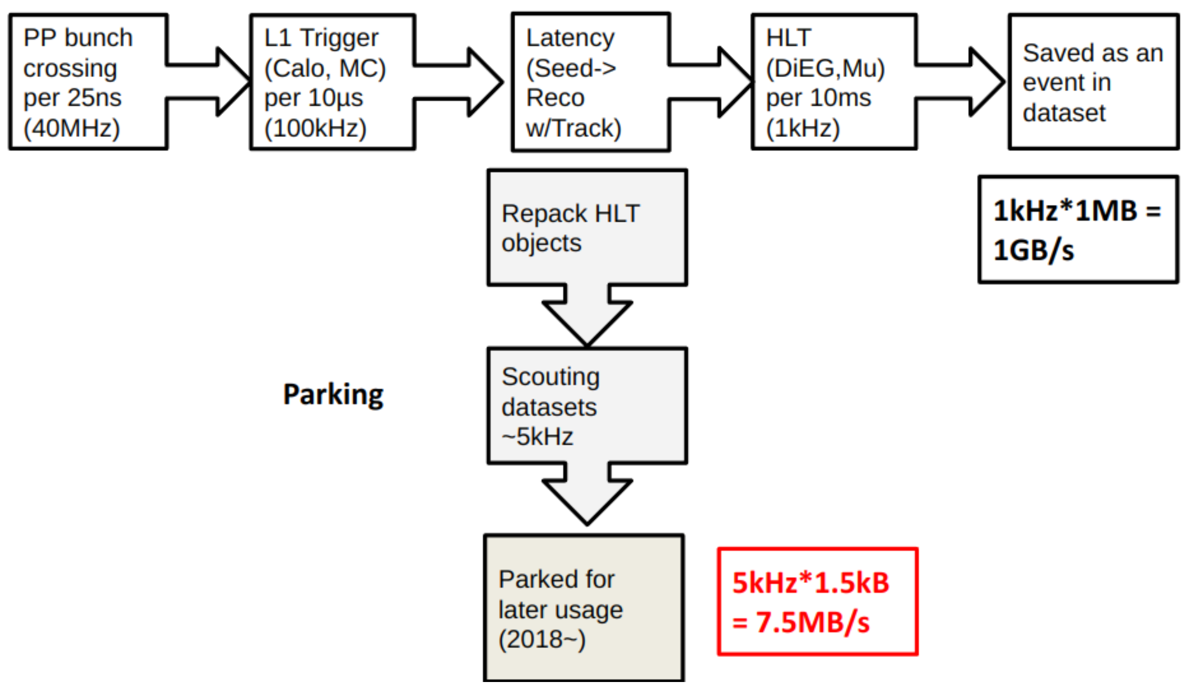

Discovery of new physics requires not only high energy, but also large statistics. New physics, for sake of not being discovered so far, has a very small cross-section. Large statistics is necessary to confirm existence of the small cross-section signal over standard model backgrounds. In order to achieve the high statistics, the CMS beam crossing happens at a very high rate with bunches of protons shooted together. CMS beam crossings occur in the CMS detector at a rate of 40 million per second (40MHz) with spacing of 25ns, while 25-50 bunch crossings are usual in Run 2 of CMS. It totals at about 1 billion events occurring in the CMS detector per second.

Proton-proton interactions are very messy and produce many tracks given its QCD nature. However, most of the events are ”not interesting” to be even considered as candidates of potentially interesting events. These events occur too quickly to be recorded and would take up vast amounts of disk space to store, which would be waste of electronic resources. In order to filter and save only ”interesting” events in the extreme environment, CMS employs the Trigger and Data Acquisition System. It selects the most interesting hundred or so events for storage with fast electronics and resolution. The CMS Data Acquisition System and Triggering are described below.

The first level of triggering, Level 1 (L1), is a hardware trigger. It uses hardware processors to rapidly select or reject events based on information from the ECAL and Muon Chamber. The Level 1 trigger reduces the event rate from 40MHz to 100kHz. An event passing the L1 trigger is transmitted to the Data Acquisition System. In addition, latency is invoked in CMS such that data-taking or additonal L1 trigger does not happen until the full Trigger and Data Acquisition System is finalized. The passed event is reconstructed by the CMS Software (CMSSW) with information from the 16M channels in the CMS subdetector systems. It also prepares the passed event in form of being scouted, which can be parked into a dataset. This strategy is implemented for physics process where the physics event happens quite frequently such that the CPU does not have capacity to store all the information with full reconstruction, but worth revisiting due to its characteristic.

Events, which passed L1 trigger, is subject to the High Level Trigger. The High Level Trigger (HLT) is a software-based trigger. The HLT decision reduces the event rate to about 1kHz for storage with processing time about 40ms per event. It uses tracker information as well and requires more stringent pt,η cut on triggering objects. An event, which passed specific HLT, is saved into the HLT's dataset and publicly available to CMS collaborators for their analysis purpose. This corresponds to about 12 Petabytes of data to be recorded by CMS annually when running at designed luminosity.

A rough schematic of trigger and data acquisition process is depicted in figure 3.9.

CHAPTER 4

B PARKING TRIGGER STRATEGY

The analysis' signal process contains displaced SM τ leptons in its final state. In order to exploit the leptonic decay of τ lepton with significant IP, specifically with muon final state for clean signal, the B-Parking triggers are used. CMS implemented the B-Parking trigger since the year of 2018 of Run 2 for research on lepton universalities. As described in chapter 3, lepton universality tests claim that interaction between leptons and a gauge boson measures the same for each lepton. In mathematical expression, R(K^*,D^*) defined as in formulae 4.1 and 4.2, are tested.

$$R(K^*) = \frac{B- > K^*\mu^+\mu^-}{B- > K^*e^+e^-} \tag{4.1}$$

$$R(D^*) = \frac{B- > D^*\tau^\pm\nu}{B- > D^*\mu^\pm\nu} \tag{4.2}$$

The first ratio specifically attracts investigation of many physicists. R(K^*)'s physics process is highly suppressed due because Flavor-Changing Neutral Current (FCNC) is not allowed in the SM. For a b-quark to change its flavor to strange quark, it has to go through a loop process with 2 additional vertices, making the cross-section highly suppressed. Di-muon and di-electron signature of the highly suppressed process is very clean, making it optimal channel to test lepton universality, Its Feynman diagrams are shown in figures of 4.1 and 4.2 Because of this physics reason, muonic final state of B mesons are desired for research of R(K^*,D^*), . Consequently, B-parking trigger requires a soft muon with modest displacement (measured using impact parameter) from the primary vertex, as in b-tagging, by exploiting the b-quark's long lifetime. It requires a muon with transverse momentum (pT) of 7-12 GeV with impact parameter (IP) significance 3-6.

pp collisions in LHC produce extremely enormous amount of events, which could trigger the B parking trigger paths. As discussed in chapter **??**, Current CPU capacity of CMS is limited and not capable of reconstructing the entire event at such high trigger rate in HLT level. Thus, CMS scouts events, meaning it writes events that passed L1 trigger to a temporary dataset. Later, full HLT and RECO steps are implemented and served as a B-Parking dataset. The prescale factor for BPH triggers is 5-6.

Figure 4.1: The figures show two different loop diagrams for B$->K^*l^+l^-$ processes. The FCNC is forbidden in the SM and there is no tree level process for B$->K^*l^+l^-$. Thus, these two processes are the leading contributors for B$->K^*l^+l^-$, which are highly suppressed.

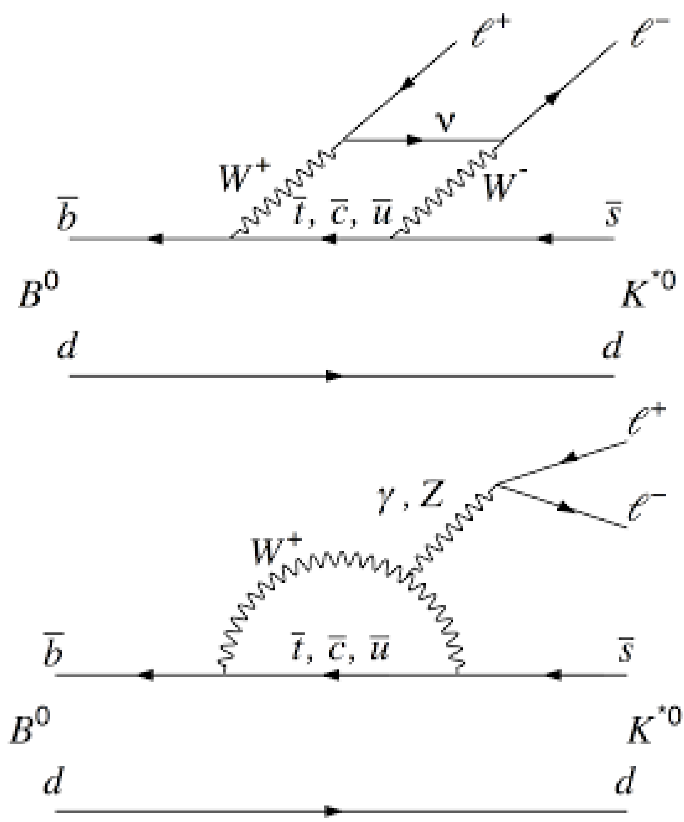

4.1 Trigger Paths

We use data collected by the B-Parking triggers for the year of 2018. The exact names of paths for B-Parking triggers are listed in Table 4.1.

Below is the trigger efficiency of various BPH trigger paths for different mass and lifetime points of the signal (HToSSTo4Tau) sample Signal process shows an overall good efficiency. Signal points with LLP's cτ = 10,100mm show the best performance. Signal points with LLP's cτ = 1000mm likely decays outside of the tracker region, leaving no track's impact parameter, and fails to pass the trigger. On the other hand signal point with LLP's cτ = 1mm may not reach the first pixel detector, which is at 2.7cm from the beam spot, and fails to pass the trigger. We can confirm this explanation with observation that lighter LLP's MS has better trigger efficiency for shorter lifetime thanks to higher boost, and the vice versa for heavier LLP's MS.

Figure 4.2: If the Lepton universality is not satisfied (R(K*,D* $\neq$ 1), it implies there is new physics hidden in the diagram. It could be interpreted in terms of Lepto-quark or Electroweak Z boson which couples to right-hand chrial leptons.

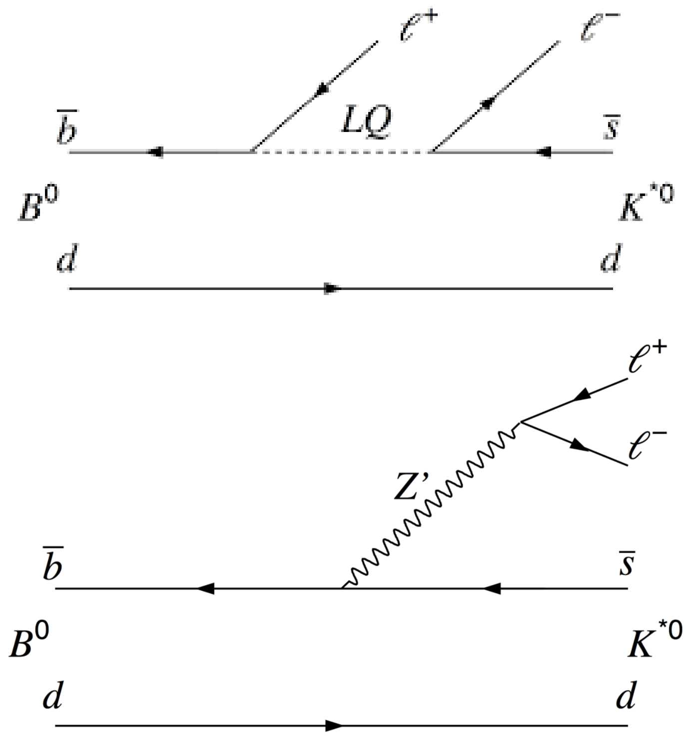

In contrast to the signal, the background process shows a poor trigger efficiency. Drell-Yan process and W-Jet process show an even poorer trigger efficiency due to absence of heavy flavor particles in its final state. TTJets, Single Tops, and QCD-MuEnriched passes the trigger at better efficiency. All these background processes have heavy flavor particles for its final state (b-quark or top quark). QCD-MuEnriched has better efficiency for higher Pt bin samples, since higher Pt and HT bin samples tend to have more b-jets for its final state as well.

4.2 Integrated Luminosity and pileup weight for the HLT path

The integrated luminosity for each era has been summarized in table A.1 in Appendix A. The information was obtained with commands in section A.1 in Appendix A as well. The integrated Luminosity totals at $44fb^{-1}$ lower than $58.7fb^{-1}$ for the year of 2018 due to prescaling. The bunch-

Table 4.1: HLT trigger paths used in the analysis 2018.

Data sample	Trigger
ParkingBPH*-Run2018A	HLT_Mu9_IP6_part*
ParkingBPH*-Run2018B	HLT_Mu9_IP6_part*
ParkingBPH*-Run2018C	HLT_Mu12_IP6_part*
ParkingBPH*-Run2018D	HLT_Mu12_IP6_part*

Table 4.2: Data and MC Global tags used 2018

Data 2018	106X_dataRun2_v29
MC 2018	106X_upgrade2018_realistic_v11_L1v1

Figure 4.3: The plots show the trigger efficiency for each HLT path with respect to LLP's lifetime. Each line denotes mass scale of each scalar.

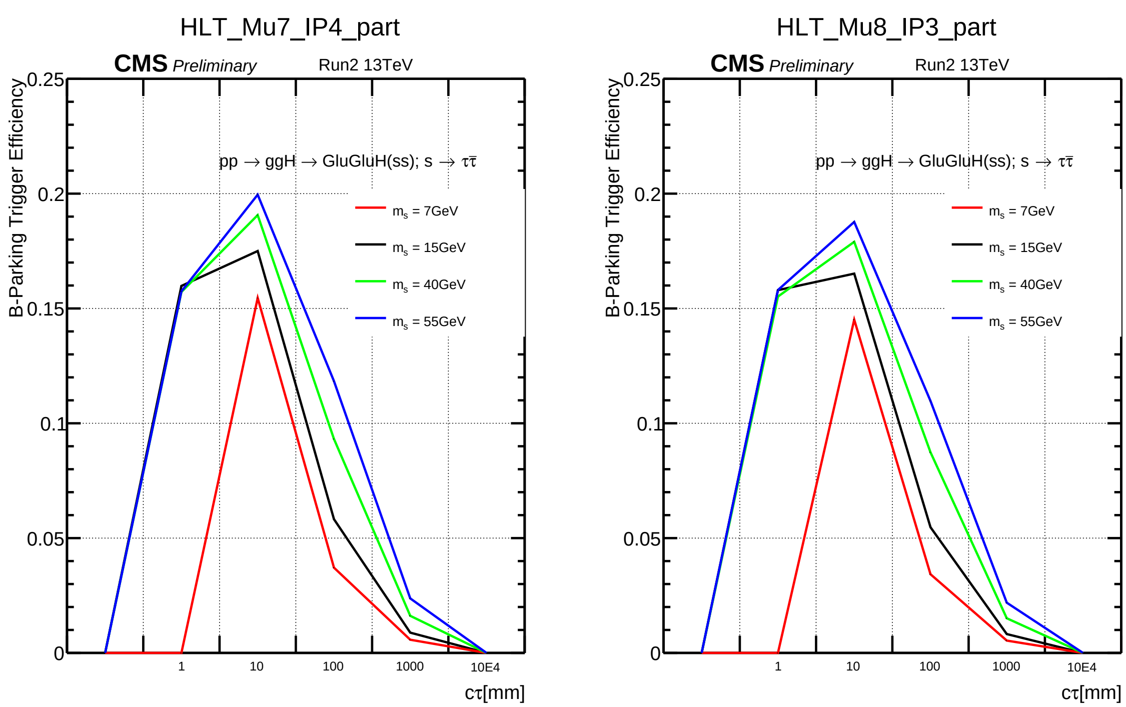

crossing for B-pakring HLT path is also very different form other HLT paths. B-parking data are recorded during lower bunch-crossing runs as expected, due to its extreme rate in the CMS collider.

To model Monte Carlo (MC) simulation correctly to describe data, it is vital to adjust this

Figure 4.4: Theese plots also show the trigger efficiency for each HLT path with respect to LLP's lifetime. Each line denotes mass scale of each scalar. The analysis uses Mu9_IP6 for Era A,B of data and Mu12_IP6 for Era C,D of data

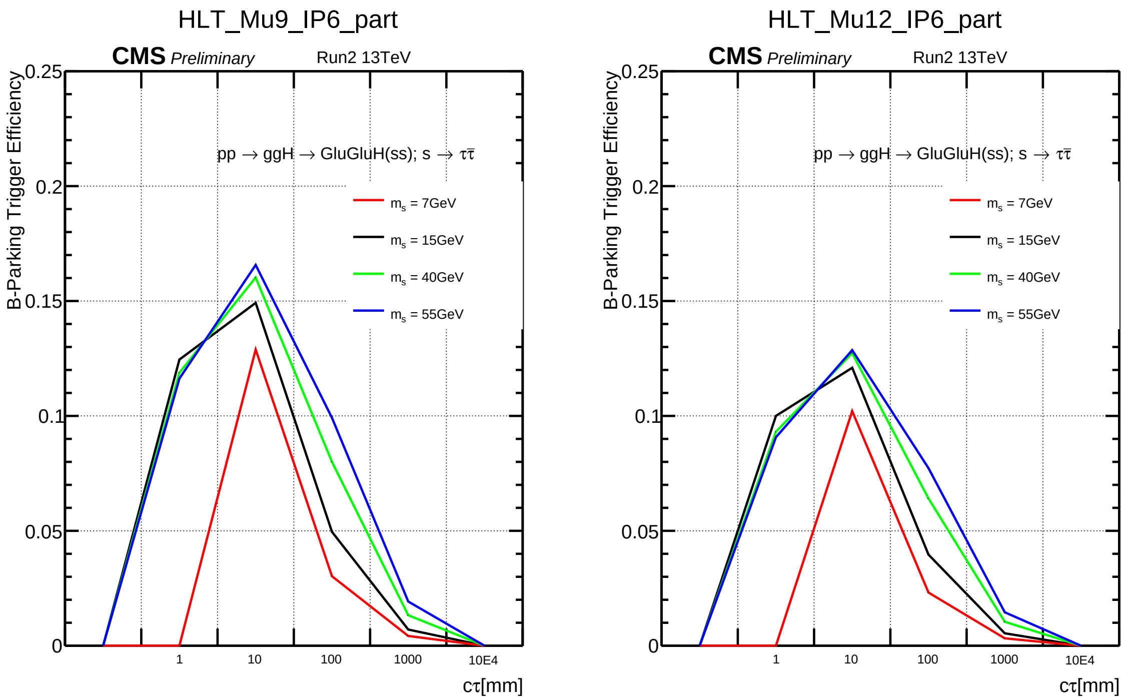

bunch-crossing variable. To achieve the purpose, we apply pileup weight on the MC simulation. Pileup weight is simply a bunch-crossing of data divided by the bunch-crossing of MC for a specific era. Pileup (PU) weight values are calculated for each era of data-taking (A,B,C,D). Figure 4.5 shows the BPH1-Era A's HLT_Mu9_IP6 HLT path's Data PU distribution.

Figure 4.6 shows the BPH1-Era C's HLT_Mu12_IP6 HLT path's Data PU distribution.

Figure 4.7 shows DYJetsToLL_M-50_TuneCP5_13TeV-madgraphMLM-pythia8 MC PU distribution.

Figure 4.8 shows resultant such PUWeight from BPH1_A HLT_Mu9_IP6 and DYJetsToLL_M-50_TuneCP5_13TeV-madgraphMLM-pythia8.

Figure 4.5: Bunch crossing of dataset /ParkingBPH1/Run2018A-UL2018_MiniAODv2-v1/MINIAOD

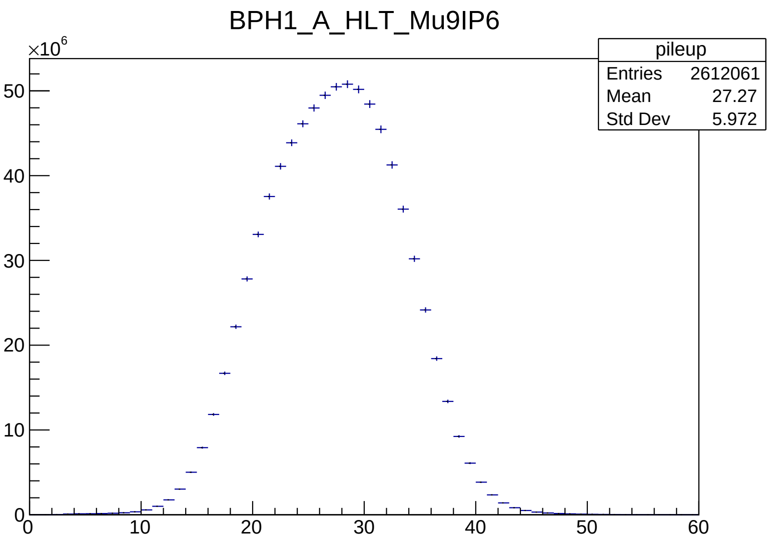

Figure 4.6: Bunch crossing of dataset /ParkingBPH1/Run2018C-UL2018_MiniAODv2-v1/MINIAOD. Please note that the HLT path for EraC has higher muon object's pT threshold with 12GeV (compared to 9GeV in EraA).

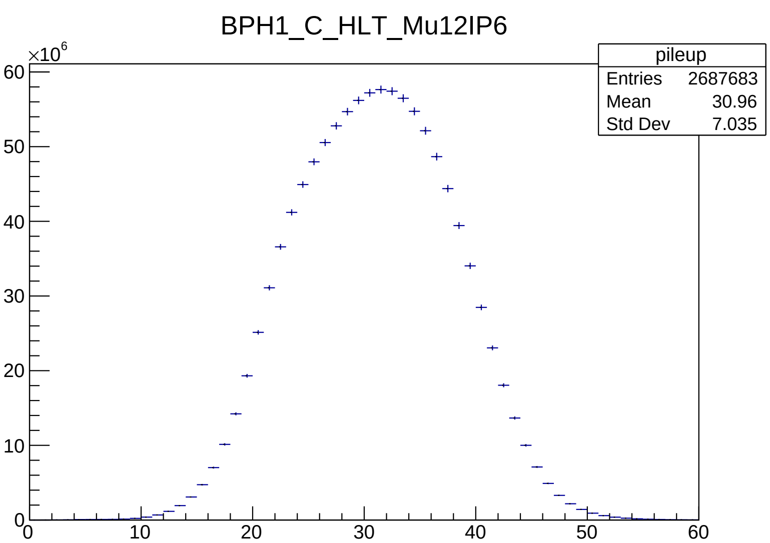

Figure 4.7: Bunch crossing of Monte Carlo Simulation for physics process of Drell-Yan. The dataset is /DYJetsToLL_M-50_TuneCP5_13TeV-madgraphMLM-pythia8/RunIISummer20UL18MiniAODv2-106X_upgrade2018_realistic_v16_L1v1-v2/MINIAODSIM

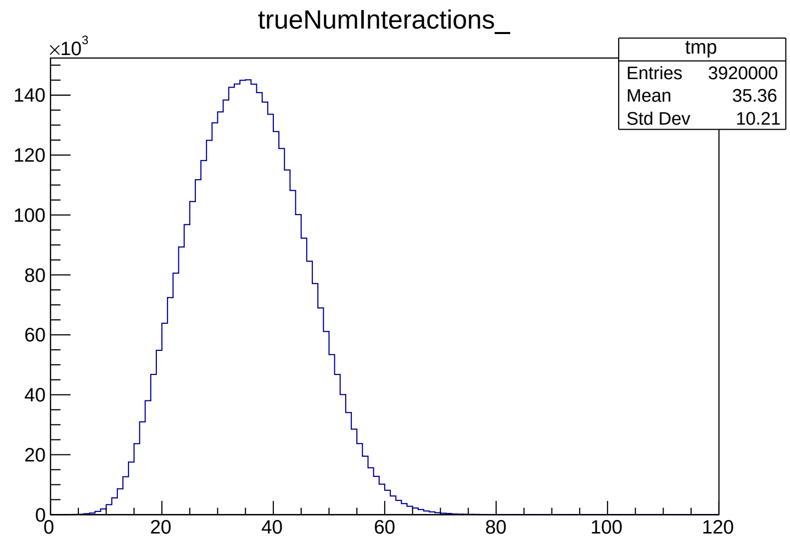

Figure 4.8: PUweight calculated for Era A of B-parking dataset

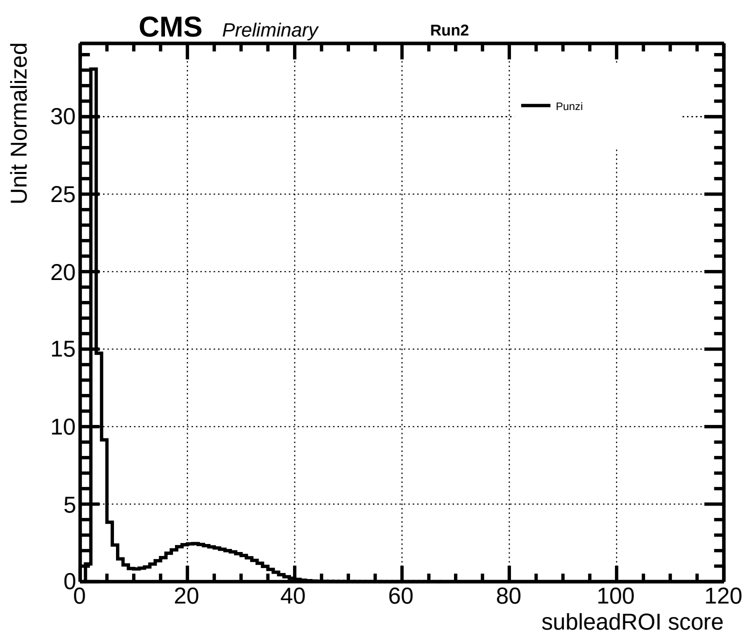

CHAPTER 5

PHYSICS OBJECT DEFINITIONS

In this section, we provide the definitions of physics objects used in the analysis. The analysis uses 2 main CMS reco objects: muons, jets. Photons do not show anywhere in our signal process. τ's of our signal process can decay into electrons with same probability as into muons. However, the analysis uses b-parking and only targets the muon decay mode of the tau. Electrons are not interest of our analysis either.

Although the signal's final decay involves τ lepton, we do not use the CMS reconstructed τ. Given that τ decay results into many different objects (muon, electron, and different combinations of hadrons) as shown in figure 1.3, the CMS uses a special reconstruction algorithm for τ object. Particle-Flow jets (PFjets), which are jets with all particle identification information within the jet, are the starting point for the τ reconstruction. With π^0 reconstructed in ECAL as a strip, the Hadronic-Plus-Strip (HPS) algorithm reconstructs τ (at 60% efficiency in Run 1) when a charged hadron and a strip is reconstructed in the PFJet [60]. Our signal process tau lepton decays into muon, in a leptonic mode, for the trigger. For other tau leptons in the signal process, we approach purely tracker oriented method with regions of Interest for our analysis. Direct usage of tau leptons in the analysis is accompanied by division of several different sub-channels (μ,e,had), which result in 27 (3^3) different combinatorics.

We use muon leptons, jets, and only tracks (ROIs) for this analysis.

5.1 Muons

The analysis sources the SlimmedMuons collection from the MINIAOD MC datasets to produce `selectedPatMuons`. Muon objects are required to have

- $pT \geq 12$ GeV to reach BPH trigger plateau
- $|\eta| \leq 1.5$ for L1 seed $|\eta|$ cut in BPH trigger
- reco::Muon object matched to the BPH trigger object
- Pass the Loose ID criterion (isLooseMuon) as described in the Muon POG [61].

The motivations for isolation requirements on muons are further discussed in Section 7.

Figure 5.1: Data/MC of muon objects pT and η

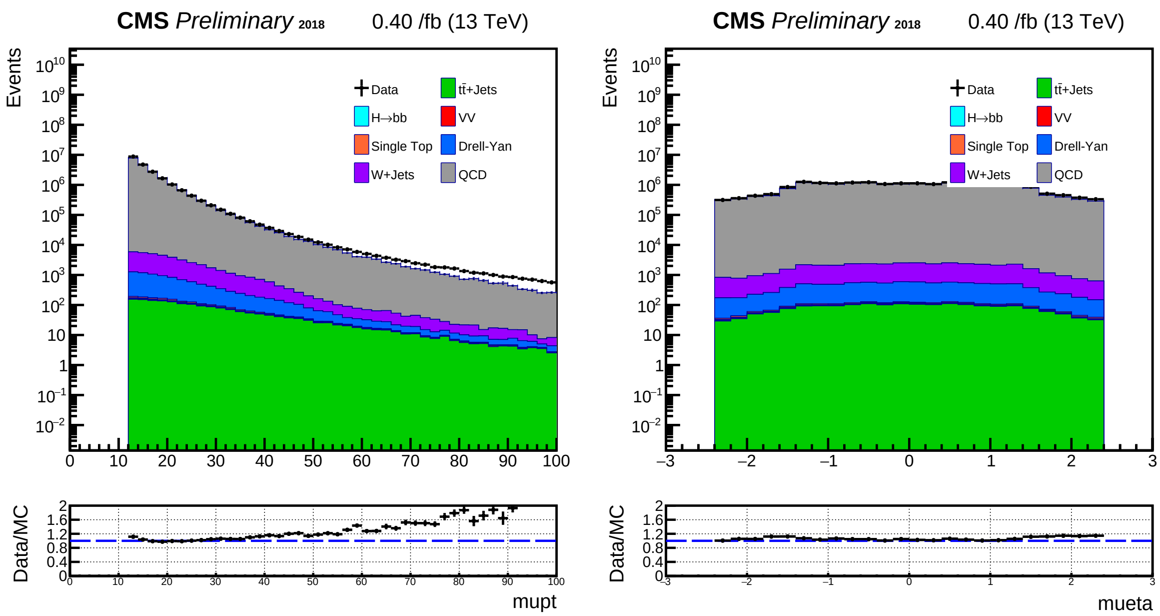

5.2 Jets

The analysis sources SlimmedJets collection from MINIAOD dataset to produce `selectedJets`. CMS reconstructs jets from calorimeter energy deposits using the anti-k_T clustering algorithm with a distance parameter of $R = 0.4$ [62]. Then, the calojets are inputed into the Particle-Flow (PF) algorithms to produce the PFJets collection. Variables in PFJets class are then slimmed to be saved into MINIAOD files. Jet objects require

- pt $\geq$ 20 GeV
- $|\eta| \leq 2.4$
- $0 \leq$ emEnergyFraction ≤ 0.9
- $0 \leq$ energyFractionHadronic ≤ 0.9
- No selected electron or muon within $\Delta R = 0.4$

The energy fraction cuts above are taken from the recommended Run2 Tight jet ID cuts for particle flow jets [63].

Figure 5.2: Data/MC of jet objects

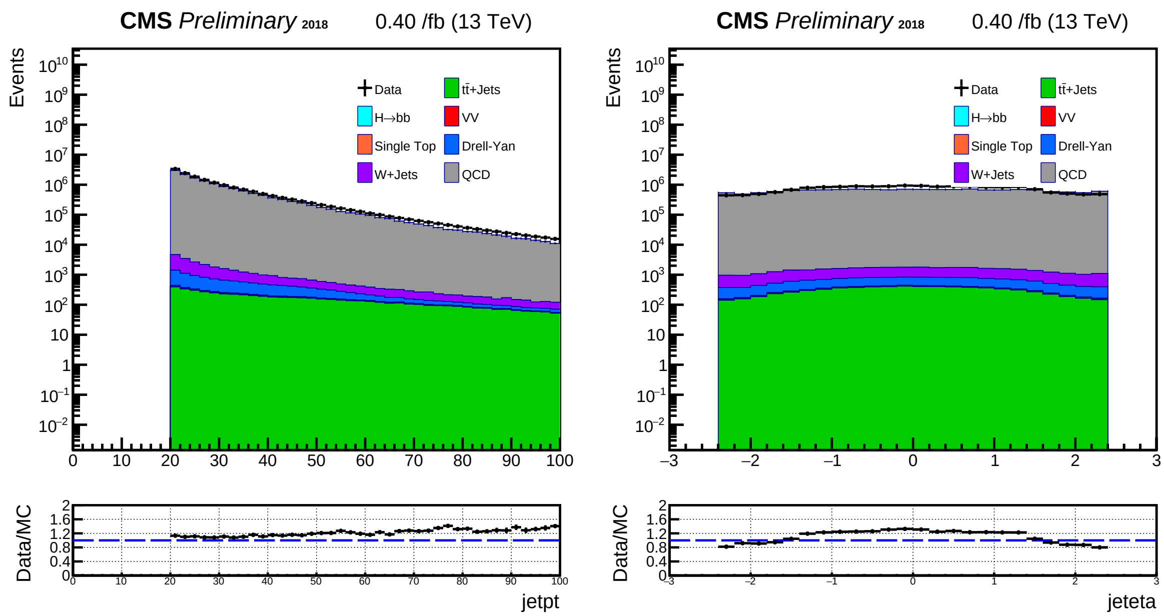

5.3 Taus

Although we do not use tau leptons for event selection or background estimation, we still plotted basic variables of tau leptons for review. The analysis sources PAT::slimmedTaus from MINIAOD for MC and RECO::slimmedTaus for Data to produce `selectedTaus`. τ's hadronic decay can be reconstructed with PFJets' charged hadrons in HCAL and 2 γs from π^0 decays in ECAL. Tau objects require

- pt $\geq$ 20 GeV
- $|\eta| \leq 2.4$

5.4 Region of Interest

Tracks contain many important qualities such as the impact parameter significance and the 4 vector. LLP scalar particles decay in the tracker, so these track qualities should be good discriminant against the background. However, we can not save all tracks in the event with all track information, as much as we have to filter out uninteresting events with trigger system in CMS. In our signal process, a geometrical concept can play a vital role to sort out only relevant tracks for our analysis purpose. LLP scalar has no electric or color charge as described in section 2. LLP

Figure 5.3: Data/MC of tau objects

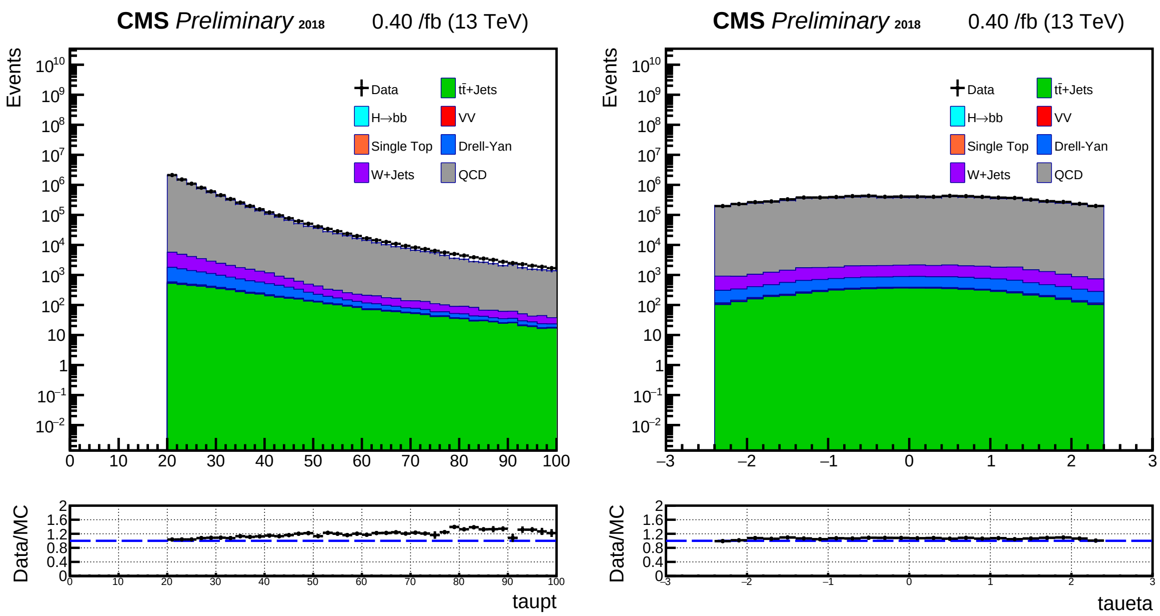

scalar leaves no tracks in the tracker, decay into 2 charged tau leptons, which subsequently decay into at least 1 charged track (μ, electron, at least 1 charged hadron). Like in the pair production, 2 charged tracks often travel opposite in their direction. Thus, a geometric convergence of 2 charged tracks should point to the decay vertex of the neutral LLP. The tracker algorithm that we use to construct this "Interesting Geometric Region" provides us a converged vertex, and the area around this vertex is referred as "Region of Interest" (ROI). The complete reconstruction procedure of Regions of Interest is detailed in the following subsections.

An ROI requires

- Good quality track selection
- Vertex Fitted from pair-wise tracks by V0Fitter in CMSSW
- Cluster the fitted vertices to form a Region of Intrest (ROI)
- Look for tracks around $\Delta R = 0.3$ around ROI to save its isolation information

5.4.1 Tracks

The analysis sources packedPFCandidates and lostTracks from MINIAOD. Track parameters and convariance values will be propagated along the ROI production process and no value should be non-physical

- !isinf(tracks.parameter) and !isnan(tracks.parameter)
- !isinf(tracks.covariance) and !isnan(tracks.covariance)
- Number of valid hits > 3
- pt ≥ 0.35
- Track $IPSig_{XY}$ $\geq$2.
- Track $IPSig_{Z}$ $\geq$-1.
- Track normalized χ^2 $\geq$10.

5.4.2 Vertex Fitter

The analysis sources offlineBeamspot from MINIAOD for beamspot reference. Vertex fitter is KalmanVertexFitter with vertex cuts as below.

- Vertex χ^2 $\geq$6.63
- Transverse Decay distance significance$\geq$15.
- V0mass $\geq$13000GeV
- cos(θ_{XY}) between x and p of V0 candidate $\geq$ 0
- cos(θ_{XYZ}) between x and p of V0 candidate $\geq$ -2

5.4.3 ROI formation

Fitted vertices are clustered to form a Region of Interest (ROI). The clustering steps can be further detailed as below.

- A fitted vertex is merged with another vertex if they are within 1cm.
- A new ROI is formed where the position vector of ROI is averaged.
- Clustering is repeated until there is no other vertex within 1cm limit.

Although vertex clustering can be done with the step above, we can be creative and acquire more information. Isolation, containing information about the ROI's environment, could also be a useful information. We can obtain information about isolation by defining an isolation shell. The shell's construction step is described as below.

- A cone of DeltaR ¡ 0.3 around the center of the ROI is defined, where DeltaR is calculated with respect to the PV.

- A plane that is perpendicular to the axis of the cone and that contains the center of the ROI is isolation plane. It becomes a circle.
- You make the circle into 3D sphere.
- Any tracks that pass through that sphere but not through the ROI are the annulus tracks.

With these crucial tracks' information, we are ready to discriminate signals from the background.

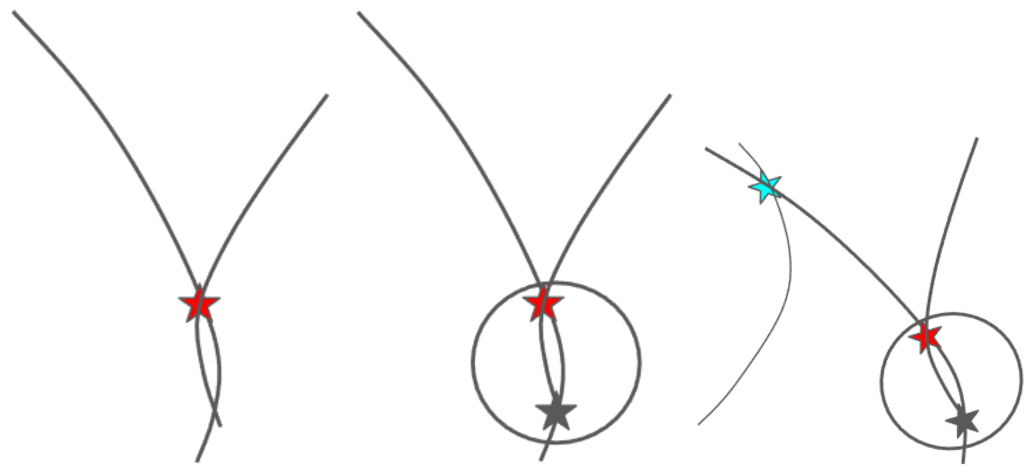

Figure 5.4: The figures display cartoons of step-by-step formation of the Region of Interest (ROI). Dark like denotes a charged track: a muon track or electron track, or a charged hadron track from a tau lepton decay. Left figure shows the vertex (red color) fitting by KalmanVertexFitter in CMSSW, from two charged tracks which decayed from a neutral LLP. Middle figure shows clustering of the region of vertex, with vertex (grey) formed by the extended tracks being clustered into original ROI, if the vertices are within 1cm limit. Right figure shows non-clustering of vertex (sky), if the verex is out of 1cm limit. The track (thinner line) which forms non-clustered vertex is most likely from a pileup interaction.

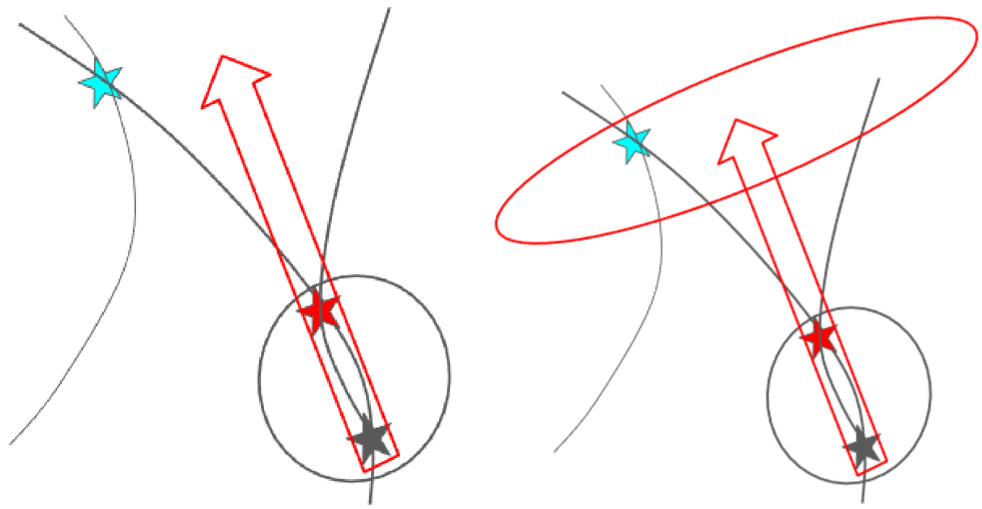

Figure 5.5: The figures display cartoons of step-by-step formation of the shell structure. Left figure shows the axis of the cone, when the axis goes through the center of ROI. Right figure shows the construction of the isolation plane, shown in red color of circle. The isolation plane has ΔR=0.3. You can see the pileup track goes through the isolation plane in the cartoon. Thus, the shell formed by this isolation plane containes information about isolation variable.

Figure 5.6: Data/MC of ROI distribution

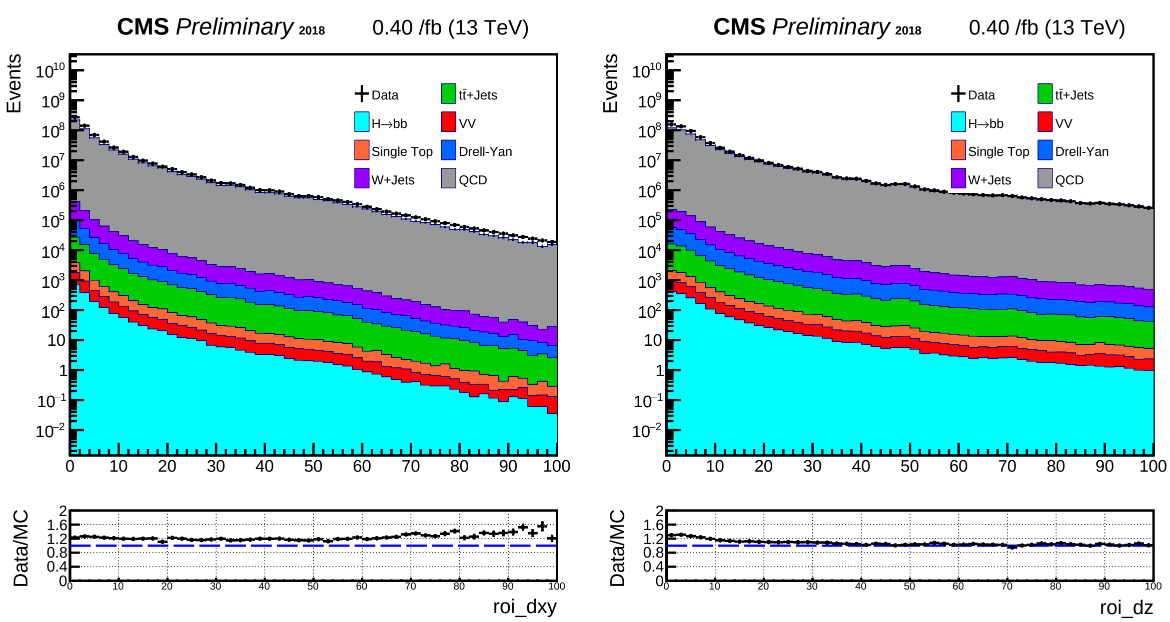

Figure 5.7: 2Data/MC of ROI distribution

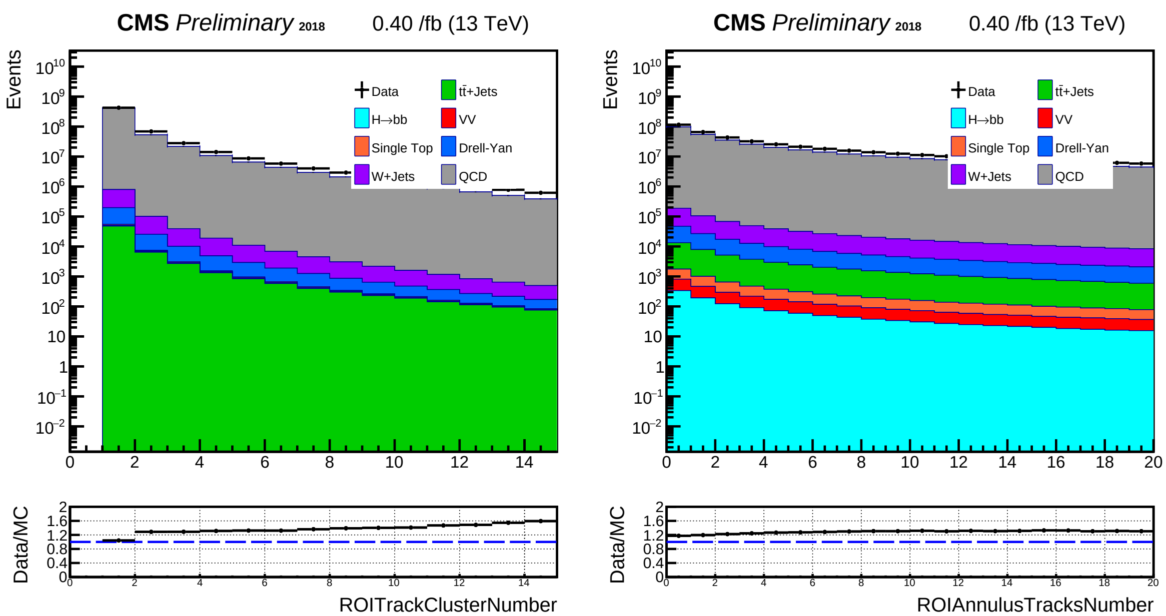

CHAPTER 6

MACHINE LEARNING

ROIs are artificial regions created by the CMSSW mechanism, which are displaced vertex candiates. ROIs contain thorough information about fitted tracks, vertices, and isolation information, after following the formation procedure described in the previous section. The exhaustive variables saved in each ROI contain information, which directly and indirectly tells whether the ROI is from signal process or background process. Given the extensive amount of variables within ROIs, it's inappropriate to use ROIs' single or a few variabes as our tagging variables, like in ZH analysis [45]. It is also ineffcient to implement a cut-based approach due to having approximately 20-30 variables from ROI. Optimization process for all 20-30 variables would be extremley time-consuming, inefficient, and error-prone as well. Therefore, the analysis exploits machine learning (ML) for these multivariate analysis. Boosted decision trees will also face similar problem as cut-based analysis, although to a lesser extent. Deep Neural Network are the most adaptable ML algorithm for this analysis method, in which the algorithm inputs extensive list of ROI variables into a neural network, and receives a final score to discriminate ROIs that arise in signal process versus background processes. The list of variables that are inputted into the ML algorithms are provided in subsection 6.1.

The analysis uses Keras-Tensorflow for its ML platform. CMSSW includes Keras-Tensorflow, which enables simple and easy usage of keras-Tensorflow with simple cmsenv command in various CMS remote clusters. For CMSSW_10_6_12 (to have access for BPH trigger path), Keras-Tensorflow version is 2.3.1. It runs with CPUs and GPUs.

6.1 Machine Learning Input Variables

As discussed in chapter 5, the ROI has vertex and shell (isolation) information. Vertex information is trained with 19 different variables, which are listed and categorized in Tables 6.1.

Shell information is trained with 8 different variables, which are listed in Tables 6.2.

We input vertex and shell information into separate ML algorithms. Thus, we get 2 final products from the ML algorithms, one for the vertex and the other for the shell.

Table 6.1: ROI (trackCluster) variables by category

TrackCluster	Position	TrackClusters.vx() - primaryVertex.X()
	Position	TrackClusters.vy() - primaryVertex.Y()
	Position	TrackClusters.vz() - primaryVertex.Z()
	Covariance	TrackClusters.vertexCovariance()(0,0)
	Covariance	TrackClusters.vertexCovariance()(0,1)
	Covariance	TrackClusters.vertexCovariance()(0,2)
	Covariance	TrackClusters.vertexCovariance()(1,0)
	Covariance	TrackClusters.vertexCovariance()(1,1)
	Covariance	TrackClusters.vertexCovariance()(1,2)
	Track0,1	Track0,1.pt
	Track0,1	Track0,1.eta
	Track0,1	Track0,1.phi
	Track0,1	Track0,1.dxy
	Track0,1	Track0,1.dz
	Track0,1	Track0,1.normalizedChi2
	Track0,1	Track0,1.HighPurityInt

6.1.1 Fine-Tuning of ML environemnt

CMSSW includes image container for Keras-Tensorflow and researchers can submit remote batch jobs for its ML training as well. The analysis tested multiple variables (such as epoch numbers, batch sizes, phi sizes, f sizes) of our DNN layers thanks to submission of remote batch jobs with CMSSW's Keras-Tensorflow image container. Subsection 6.1.2 below details the numerical results from such tests. The analysis also tested different combinations of signal vs background datasets for maximum discriminant power. The list of mass scale and lifetime tested for signal points are listed

Table 6.2: ROI (Annulus) variables by category

Annulus	pfCandidate/LostTracks	pfCandidate/LostTracks.pt
	pfCandidate/LostTracks	pfCandidate/LostTracks.eta
	pfCandidate/LostTracks	pfCandidate/LostTracks.phi
	pfCandidate/LostTracks	pfCandidate/LostTracks.dxy
	pfCandidate/LostTracks	pfCandidate/LostTracks.dz
	pfCandidate/LostTracks	pfCandidate/LostTracks.normalizedChi2
	pfCandidate/LostTracks	pfCandidate/LostTracks.HighPurityInt
	pfCandidate/LostTracks	pfCandidate/LostTracks.DeltaR(trackMomentum)

in subsection 6.1.3. Different SM physics process (and their compositions) tested for background process are also listed in subsection 6.1.3

The final Tensorflow product, which was used for the analysis, were trained with parameters in the following section. With these variables, Keras-Tensorflow DNN variable information was fine-tuned for maximum Area Under the Curve (AUC) calue. Its information is listed in the table 6.3.

Table 6.3: Tensorflow information

Epoch	300
batch size	250
Phi sizes	(64,128,256) for vertex ,(32,64,128) for shell
f sizes	(256,128,32)
Signal	ggHSSTo4Tau-MS15GeV-cτ100mm
Background	QCD_Pt120-170_MuEneriched and TTJets

6.1.2 DNN Variable Test

Batch size

6.1.3 Signal and Background MC Test

For Ethan.

Table 6.4: Tensorflow information

Epoch	loss	acc	val_loss	val_acc	AUC
100	0.2161	0.9074	0.2469	0.8942	0.9387
150	0.2039	0.9120	0.2393	0.8983	0.9414
200	0.1934	0.9151	0.2523	0.8953	0.9408
250	0.1977	0.9144	0.2459	0.8982	0.9399
300	0.1738	0.9272	0.2573	0.8977	0.9387
350	0.1607	0.9332	0.2693	0.8934	0.9403
400	0.1459	0.9387	0.2823	0.8970	0.9394

Table 6.5: Tensorflow information

Signal	Background	Loss	Accuracy	AUC
ggH_HToSSTo4Tau_MH-125_MS-7_ctauS-10	QCDMuEnrichedPt5_Pt20-30	0.1852	0.9244	0.9696
	QCDMuEnrichedPt5_Pt470-600	0.1597	0.9361	0.9727
	TTJets	0.1681	0.9320	0.9680
ggH_HToSSTo4Tau_MH-125_MS-15_ctauS-10	QCDMuEnrichedPt5_Pt20-30	0.2133	0.9093	0.9598
	QCDMuEnrichedPt5_Pt470-600	0.1687	0.9306	0.9679
	TTJets	0.1838	0.9242	0.9610
ggH_HToSSTo4Tau_MH-125_MS-15_ctauS-100	QCDMuEnrichedPt5_Pt20-30	0.0747	0.9755	0.9791
	QCDMuEnrichedPt5_Pt470-600	0.1596	0.9361	0.9727
	TTJets	0.1681	0.9320	0.9680
ggH_HToSSTo4Tau_MH-125_MS-40_ctauS-100	QCDMuEnrichedPt5_Pt20-30	0.1898	0.9209	0.9695
	QCDMuEnrichedPt5_Pt470-600	0.1765	0.9275	0.9698
	TTJets	0.1576	0.9379	0.9705
ggH_HToSSTo4Tau_MH-125_MS-55_ctauS-100	QCDMuEnrichedPt5_Pt20-30	0.1898	0.9227	0.9635
	QCDMuEnrichedPt5_Pt470-600	0.1480	0.9399	0.9674
	TTJets	0.1433	0.9450	0.9706

6.2 ML scores of the ROIs

ROIs of all events inside the dataset listed in section **??** are scored with the tensorflow, when the tensorflow was trained with information from section 6.1. Because the signal process has 2 scalar decays as in Figure A.1, it's reasonable to require 2 high-scoring ROIs for our analysis. However, the 2 selected ROIs are not simply the 2 highest-scoring ROIs of the event, due to non-negligible lifetime of τ leptons (from signal process in the detector. After obtaining an ROI with highest ML output socre, we search for the next highest scored ROI that are $\Delta\Phi$¿0.4 from the leading ROI. Vertex discriminant is more powerful thatn the shell discriminant. Thus, the ordering of ROIs scores are only done by the vertex ML output value.

Figure 6.1: Tensorflow scores

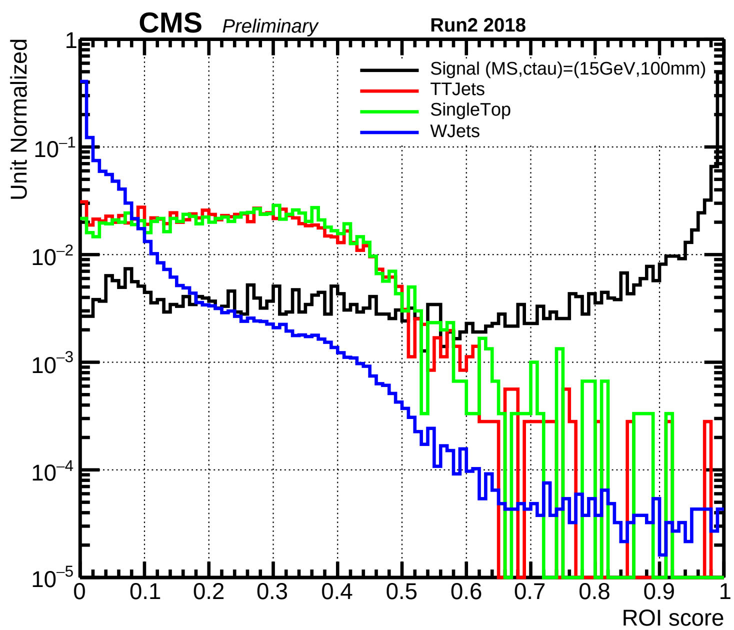

Figure 6.2: Signal versus Background for log10(1-ROIscore), where the ROI score is the highest ROI of the event. Left plot is for MS-15_ctauS-10mm point, whereas the right plot is for MS-15_cauS-100mm point

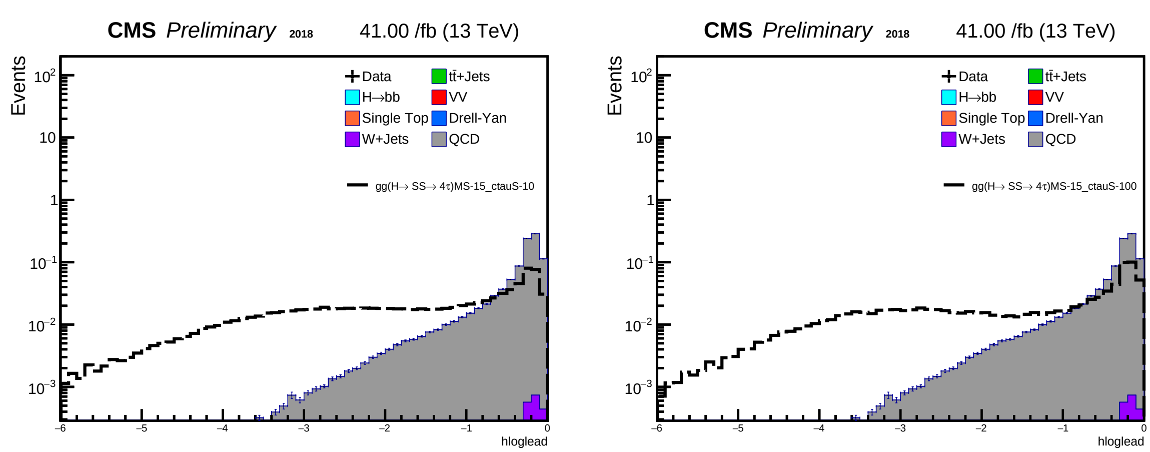

Figure 6.3: Signal versus Background for log10(1-subROIscore), where the ROI score is the second highest ROI (outside of dPhi=0.4 from leading ROI) of the event. Left plot is for MS-15_ctauS-10mm point, whereas the right plot is for MS-15_cauS-100mm point

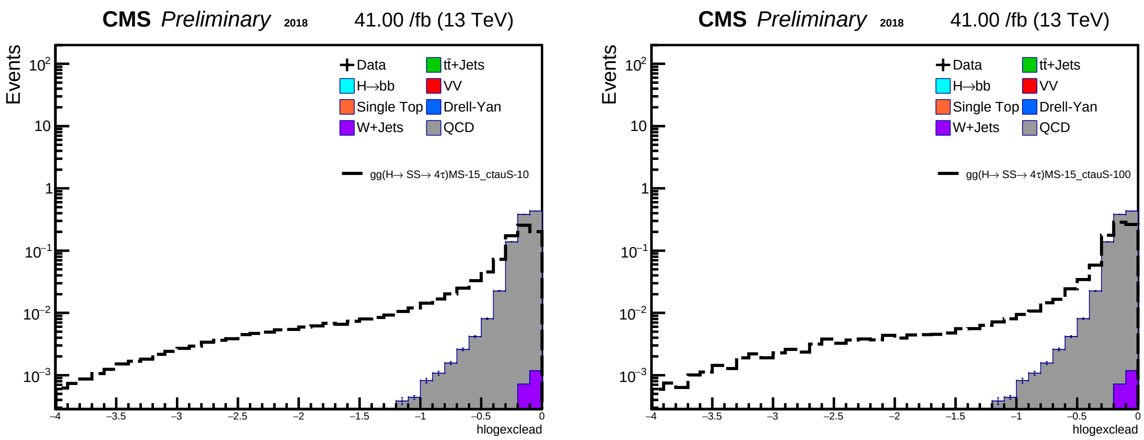

Figure 6.4: Data/MC agreement for ROI scores

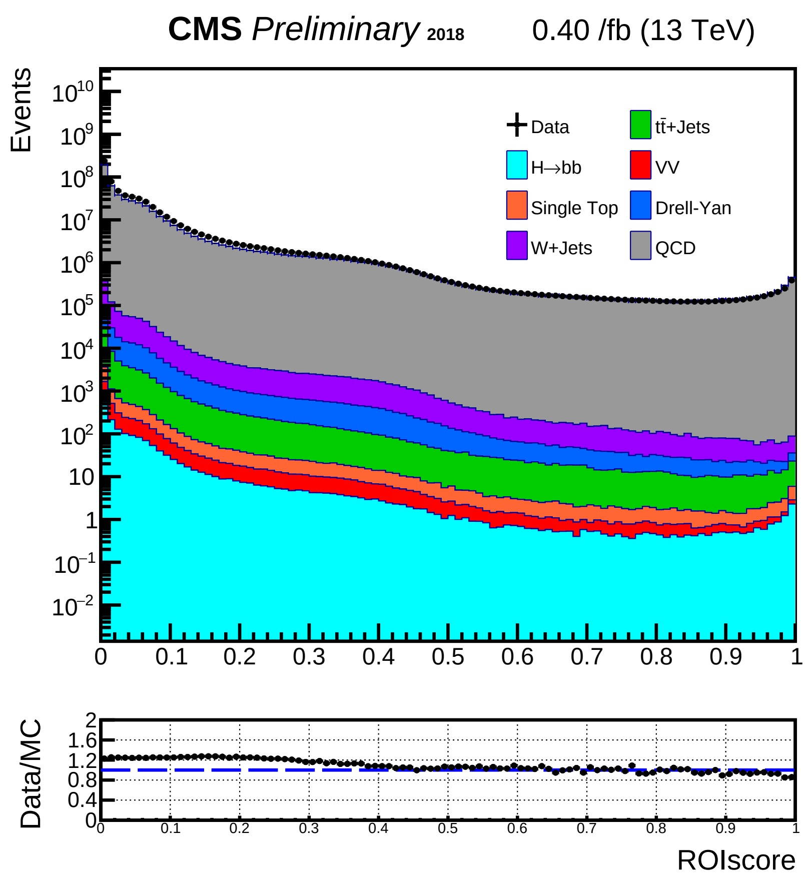

Figure 6.5: Data/MC agreement for loglead/sublead scroes

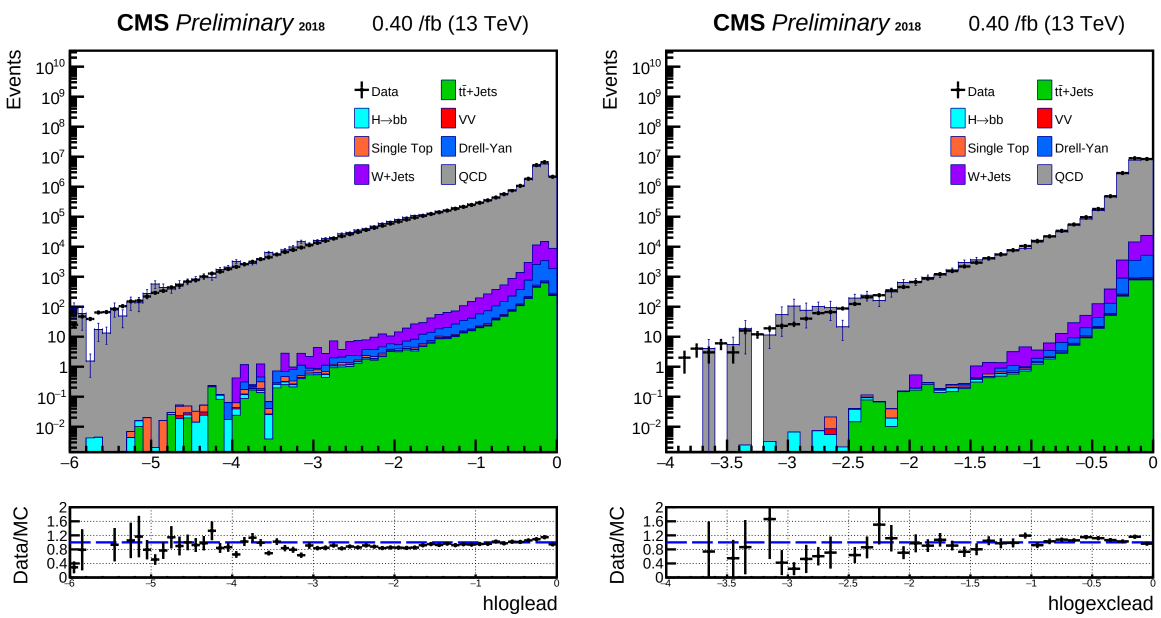

CHAPTER 7

EVENT SELECTION, SIGNAL AND CONTROL REGIONS

We have introduced the leading ROI's vertex score and subleading ROI's vertex score, which were both highly discirminant (Score ordering is based upon the vertex score). Although we might have successful event selection with just triggers, and ROI vertex scores, we could strengthen the discriminant power further if we consider objects other than the trigger and ROIs(tracks). These variables could be

- Non-relevant to ROIs (muon, jet object)
- Missing input variable in the ROI training

These are not inputs of ML training, something that can't be learned by the ML, so not discriminated with scoring of the ROIs. For this phenomenological situation, the analysis implements further event selection categories itemized below.

- $\Delta\Phi(leadROI, subleadROI)$
- $\Delta R(leadROI, Jet)$ <0.6
- 1 Isolated μ
- Leading μ's transverse impact parameter significance to PV

Each of the cuts for the items above is motivated and explained in following subsections.

7.1 Delta Phi(lead ROI,sublead ROI)

This analysis looks for displaced vertices in the tracker region, coming from the decays of exotic LLPs from Higgs produced in gluon fusion mode, leaving the SM Higgs boson without boost. The largest mass of the exotic LLPs is 55 GeV, ranging down to 7 GeV. Thus, exotic LLPs decayed from the SM Higgs become boosted, with their momentum vectors pointing back-to-back in the SM Higgs rest frame. Exotic LLPs with lighter mass are more boosted than heavier LLPs, since less LLP mass means more leftover energy into kinetic energy. Given that ROIs corresponding to an exotic LLP's decay should have the highest ROI score, one should expect that the leading ROI and subleading ROI in a single event would be back-to-back. Thus, in signal events, $\Delta\Phi$(lead ROI,sublead ROI) tends to have high values, while the background processes tend to have a more uniform distribution. This analysis applies a cut above 2.2 to reduce background contribution.

Figure 7.1: Signal versus Background for Delta Phi(leadROI, subleadROI). Left plot is for MS-15_ctauS-10mm point, whereas the right plot is for MS-15_cauS-100mm point

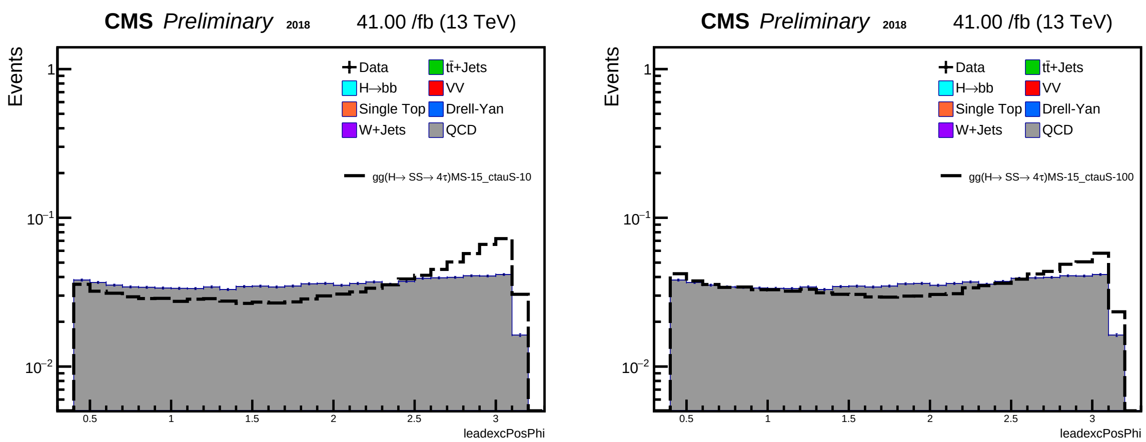

7.2 Isolation criteria for muons

As discussed in 4, the main background for our analysis comes from QCD background events, especially from B-meson decay of QCD events with high ROI scores. Leptonic decay of B-meson generates muons, which trigger the B-parking trigger of the analysis. Muons of B-meson decay have very poor isolation quality, just like ROIs formed around the B-meson decay. In contrast, muons of τ lepton decay have better isolation quality. In order to eliminate the dominant B-meson background from the QCD process, the analysis applies a PFISOLoose in selecting muon objects. The precise definition of PFISOLoose is defined as below.

- $(\Sigma pT(ch.hadfromPV) + max(0, \Sigma ET(neut.had)\Sigma ET(phot) - 0.5 * \Sigma pT(ch.hadfromPU)))/P_T(\mu) < 0.25$

Some muons decayed from τ lepton with 7 GeV mass fail isolation cut, due to its poorer isolation quality from the boost. However, it still benefits to apply the PFISOLoose cut on muons given it removes more background events than signal events. The table below demonstrates event yield

MC sample	events with BPH+1μ (noISO)	events with BPH+1μ (ISO)
15to20	1	0.545
20to30	1	0.407
30to50	1	0.295
50to80	1	0.144
80to120	1	0.078
120to170	1	0.049
170to300	1	0.032
ggH4τ-MS7	1	0.619
ggH4τ-MS15	1	0.855
ggH4τ-MS40	1	0.910

Table 7.1: Ptbinned Isocut

drop before and after requiring PFISOLoose cut on muons, classified by its signal and background process.

7.3 Leading muon's transverse impact parameter significance to PV

With the B-Parking trigger, triggering muons have significant transverse displacement (impact parameter) in both background and signal processes. However, displacement in the signal process is greater than the that of the background process. The signal process has at minimum of $c\tau =$ 1mm, which is longer than B-meson lifetime. Thus, triggering muon object's transverse impact parameter to PV is larger in signal process than background process. In order to account for the error values associated with the parameter, we use impact parameter significance defined as the ratio of impact parameter divided by its error. In order to adjust the orders of magnitude observed for the variable impact parameter significance (IPSig), we exploint log value of the IPSig. The analysis implements a cut on this variable.

7.4 DeltaR(ROI, jet)

τ leptons of the signal process can also decay hadronically, while only one of the τ leptons decay muonically to trigger B parking trigger. When τ leptons decay hadronically, its decay shower can get clustered in the calorimeter, and reconstructed as a jet. Given the τ lepton's on-shell mass is a fixed value, τ lepton and its hadronic decay products (to-be clustered into a jet) have a

Figure 7.2: leading muon's transverse impact parameter value to the primary vertex. Left plot is for MS-15_ctauS-10mm point, whereas the right plot is for MS-15_cauS-100mm point

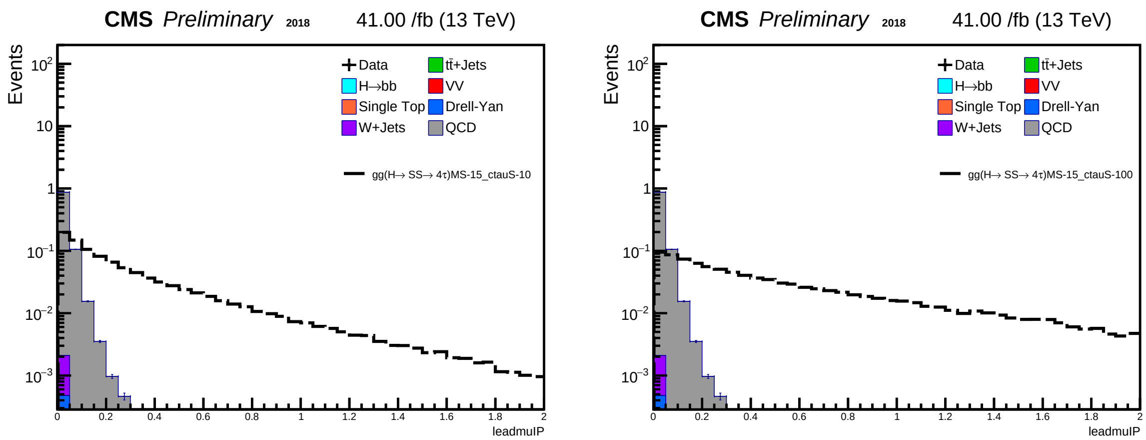

specific kinematic phase space. Thus, the Δ R(ROI, jet) has a distribution with a peak at a certain value (around 0.3-0.6). Meanwhile, the QCD backround has a different distribution shape. Given the hadronic nature of the process, jet multiplicity is high. Higher jet multiplicity makes the Δ R(ROI,jet) value to have a rather randomized value, resulting in a flat distribution.

Figure 7.3: Delta R(Jet, leadingROI). Left plot is for MS-15_ctauS-10mm point, whereas the right plot is for MS-15_cauS-100mm point

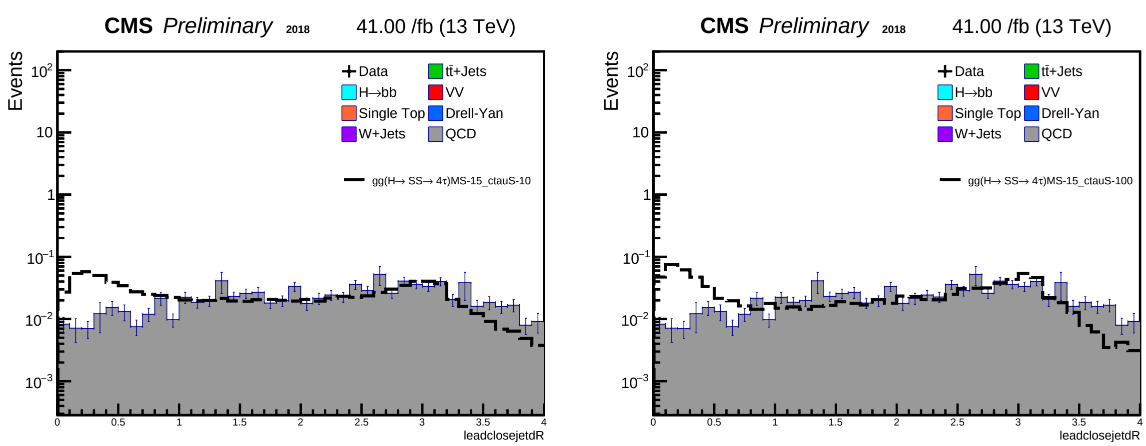

7.5 Number of Annulus Tracks Associated with ROI

The tensorflow used for this analysis is trained with p_T, η, χ^2, and other information of the annulus tracks (tracks that are inside ROI radius, but not fitted to vertex). Meanwhile, an ROI's total number of annulus tracks is not a direct input for ML and tensorflow can only learn such information indirectly via annulus tracks' p_T. Although having selected ROIs with high scores (>0.999), signal processes ROIs' number of annulus tracks show a quite different distribution from the background process. signal's high-scoring ROIs are mostly from the the exotic LLP scalar's decay into τ leptons. Since the signal's high-score ROIs' are very well isolated, the ROI's number of annulus tracks is very low. QCD background events, which are our dominant background, have a poor isolation quality. Since QCD's high-scoring ROI's are poorly isolated due to QCD nature, these ROIs' numbers of annulus tracks are higher than the signal. More precisely, QCD's high-scoring ROI's are usually from B-mesons, which have higher track multiplicity than τ leptons.

Figure 7.4: Number of tracks in the annulus cone of the leading ROI. Left plot is for MS-15_ctauS-10mm point, whereas the right plot is for MS-15_cauS-100mm point

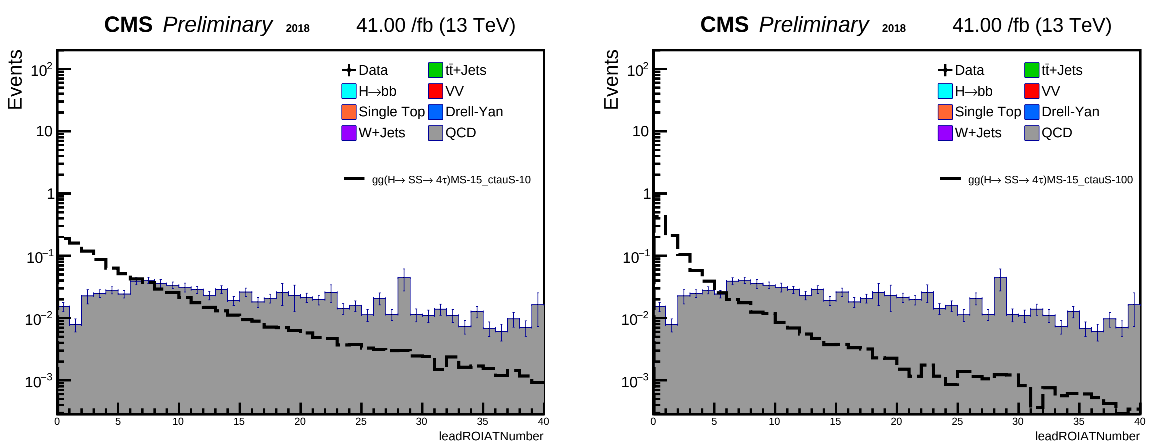

CHAPTER 8

BACKGROUND ESTIMATION

Section 7 listed several different discriminant variables for the analysis. Leading ROI vertex score, subleading ROI vertex score, and leading muon's IP value have the most discriminatory power. Although the background MC samples describe the data's distribution fairly well, one can also see discrepancy at higher vertex score and higher IPSig values. This originates from 2 different reasons. First, the lack of statistics is a fundamental deficiency for the MC samples. Unlike 11.9 billion events b-parking data, MC sample events are simulated with extremely intensive computing resources. Thus, its event number is limited below 100 milion at most, failing to describe distributions for extreme values. Second, the QCD MC's data description accuracy lacks compared to other physics process. QCD background, which is the main background for the analysis, is a quantum-chromodynamics process. QCD involves a lot of uncertainty and relies on probablistic description at low energy. Therefore, QCD's description accuracy lacks compared to other process such as WJets and Drell-Yan process. Since MC does not describe the data in a satisfactory manner, the analysis uses data-driven background estimation method.

8.1 ABCD method

For any background estimation method, ABCD method is the most preferred thanks to its simplicity. ABCD method is a simplest form of transfer-factor. A ratio of background event at 2 control region (CR) is applied to another CR's background event to infer background event in signal region (SR) without unblinding. Simplest mathematical for is described in formula 8.1.

$$SR : CR1 = CR2 : CR3, SR = CR1 * \frac{CR2}{CR3} \tag{8.1}$$

ABCD method requires 2 variables used for its estimation should be independent of each other for background process.

Unfortunately, leading ROI vertex score and subleading ROI vertex score are correlated in the QCD background process. ROIs from B-mesons score higher in our tensorflow. In QCD processes, the B-mesons are likely to be pair produced. Therefore, when the leading ROI vertex score is high due to its b-like behavior, the sublead ROI vertex score is also high because the anti-meson is produced on the other side of the detector. Thus, leading and sublead scores can't be our ABCD discriminant variable candidates due to their correlation.

The analysis selects leading ROI and leading muon's IP value as its ABCD discriminant variables. After implementing all other cuts (sublead ROI, $\Delta\Phi(lead, sublead)$, Annulus score, 1 Isolated μ, $\Delta R(leadROI, Jet)$), we tested the correlation factor between the leading ROI, and leading mu's IPSig values for each background process. The values are pretty minimal except for 2-3 processes where there were too few entries to derive a physical conclusion due to statistical limitations. Therefore, the analysis uses leading Log10(IPSig) and leading ROI vertex score for its ABCD discriminant variables.

The results are listed below.

Figure 8.1: Cutflow histogram of MS15GeV-ct100mm point. Left plot is for region A, whereas the right plot is for region D

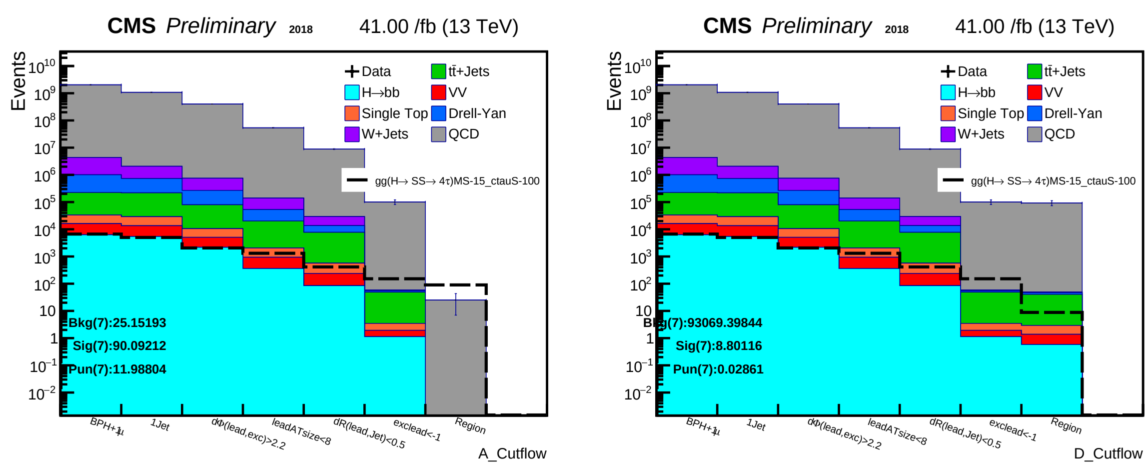

8.2 Validation of ABCD method

Although background MC's correlation factor($\hat{r}$) values are small, we need to verify that the data's correlation factor is negligible since data will be used for our background estimation. However, direct computation of $\hat{r}$(leadROI,Log10(muIPSig)) for data is problematic because the CMS community stipulates "blinding". In general, high signal ratio is expected in singal region. In order to avoid bias for new discovery and changing their analysis strategy, the CMS recommends physicists to blind themselves from looking into data entry in the signal region, until community

Figure 8.2: eee

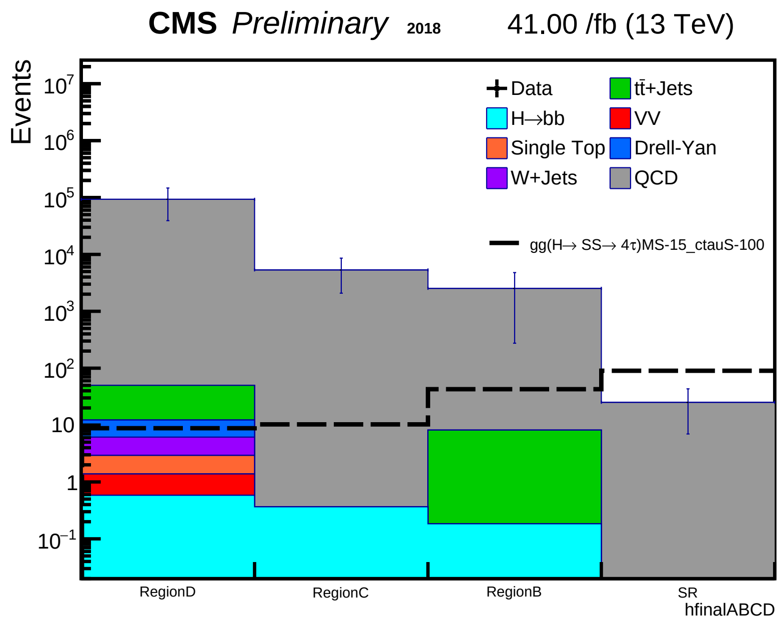

acknowledgement is granted. This concept is called "blinding" Since one can not have access for data entry in the signal region, data's correlation factor($\hat{r}$) can not be computed. Therefore, one needs to find an alternative way to estimate data's $\hat{r}$(leadROI,Log10(muIPSig)) without unblinding data in the signal region.

For this purpose, we define a new ABCD region, referred to as A'B'C'D'. A'-D' region is an orthogonal plane to the original ABCD, where the dϕ category of the event selection is flipped while all other event selection cuts are removed. Region A', a correspondant Signal region of the orthogonal plane, should be much lower in signal ratio (background dominated): Only so, looking into data entry in A' is not problematic. In figures of a-b, we confirm that background dominates the A' region while the signal entry is lower regardeless of the signal's MS and ctau.

In A'-D' region, we can see the correlation factor is about 10%, still a negligible value.

With $\hat{r}$(leadROI,Log10(muIPSig)) value in A'-D' region, It seems sufficient to claim that there should be negligible correlation between leadROI and Log10(muIPSig) for A-D region as well. Unfortunately, suspicious people could throw 1 last question. What if $\hat{r}$(leadROI,Log10(muIPSig)) value changes with respect to dϕ? If the formula in **??** is not true, $\hat{r}$(leadROI,Log10(muIPSig)) obtained from A'-D' is not a good estimate for $\hat{r}$(leadROI,Log10(muIPSig)) for A-D.

$$D_\mu = i\partial_\mu - \frac{1}{2}g\tau * W_\mu - \frac{1}{2}g^{'}YB_\mu \tag{8.2}$$

To check that formula **??** is true, we subdivide A'-D'. A1'-D1' are orthogonal planes where dϕ is closest to A-D. Increasing numeric value indicates how far the dϕ is from the A-D. $\hat{r}$(leadROI,Log10(muIPSig)) value for each of A'-D' region is plotted in figures and summarized in table.

As we scan $\hat{r}$(leadROI,Log10(muIPSig)) for each dϕ section, very small trend with respect to dϕ is observed. We can claim the formula **??** is true and $\hat{r}$(leadROI,Log10(muIPSig)) from A'-D' can be translated into A-D region as well.

Since there is not correlation of 2 variables for ABCD region, we validated the background estimation method. With background rate in signal region estimated by ABCD method with data, and with signal MC, we can either claim there exists signal over the SM expectation or not. If it does not, we can claim an exclusion limit on the branching ratio of the signal to a certain value.

Before that systematics

CHAPTER 9

SYSTEMATIC UNCERTAINTIES

Table 9.1 shows a summary of the systematic uncertainties included for the exclusion limit calculation,

Table 9.1: Systematic Uncertainty Table

Uncertainty	Signal (%)	Background (%)
Luminosity	2	2
Muon ID,ISO Scale Factor	2	2
ROI Score	10	-
Background Estimation Method	20	-
Statistical error	1-10	30

CMS records the delivered luminosity, which is accompanied by its own uncertainty. This uncertainty is universal and applied to every analysis. For data collected in 2018, the luminosity uncertainty are found to be 1.8%, which is applied to both signal and background. The analysis uses muon objects, which are applied with Loose ID and ISO criteria. Lepton ID,ISO scale factors, which are provided by the muon POG [61], also carry uncertainty, albeit the magnitude being minimal. The ROI score uncertainty is obtained by adjusting the leading ROI's vertex score As discussed in chapter 8, we validated the ABCD method using a validation region of A'-D'. Correlation factor of 2 variables in A'-D' was found to be a small value of 11%. This tells us that there could be 11% or slightly larger correlation in A-D region. Positive correlation implies more background concentrated in the SR(A) than its estimated rate(B*C/D), which would be about 11%. To be conservative with the estimation method, we set uncertainty sourced by the background estimation method at 20%. Last, out signal MC in SR(A) has enough statistics. However, it is not infinite. Therefore, we need to consider statsitical error of the signal MC in signal region. We have 100 events in signal region A, which results in 10% of statistical error from $\frac{\sqrt{N}}{N}$, $\frac{10}{100}$. Likely the background rate in the SR A is calculated with B*C/D. Its propagated statistical uncertainty is @@@%

CHAPTER 10

RESULTS

Unblinded result data no excess over the standard model prediction. Exclusion limit plot. Results

Figure 10.1: Current Preliminary limit plots

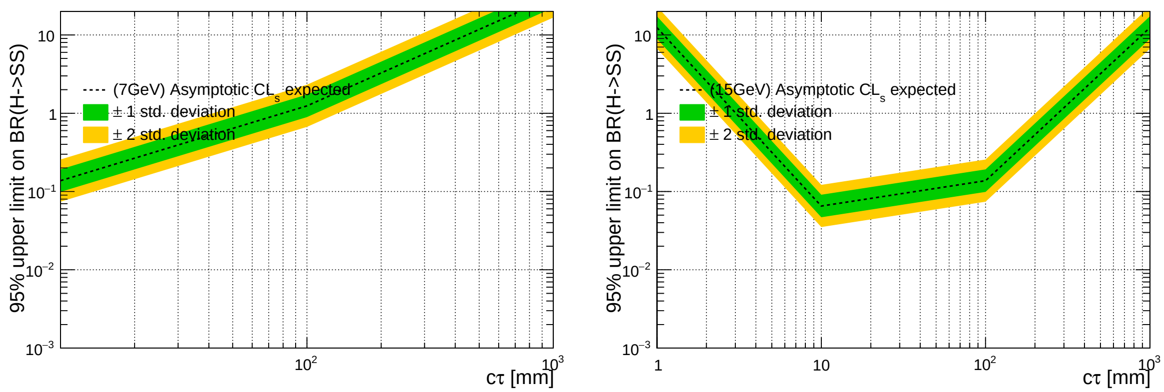

Figure 10.2: Current Preliminary limit plots

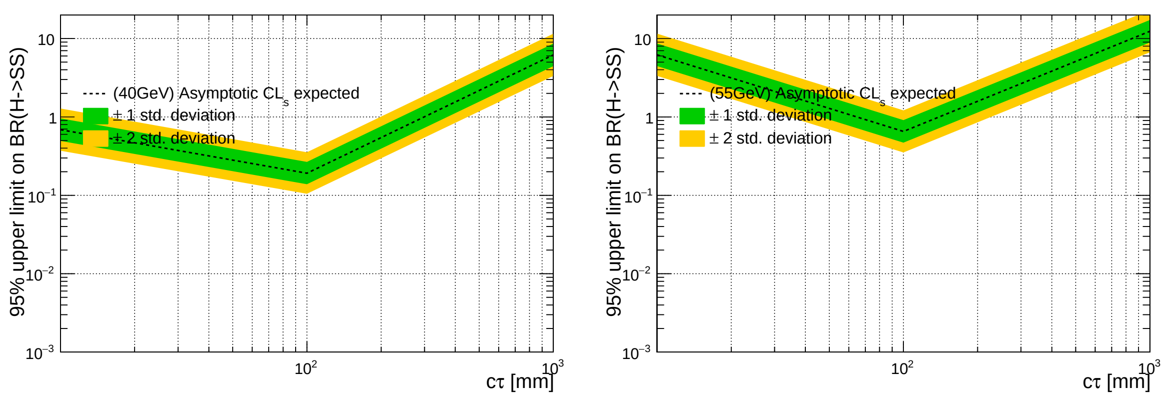

CHAPTER 11

CONCLUSIONS

This was an interesting analysis targeting tau lepton final state with tracker lifetime

APPENDIX A

DATA SAMPLES

This appendix is here merely to demonstrate how appendices may be included and formatted in your document. Look through the files `thesis.tex` and `appendix.tex` to see how these pieces work together.

The analysis uses B Parking datasets. Data was collected during the 2018 portion of Run 2 and corresponds to an integrated luminosity of 50 fb^{-1}.

A.1 BrilCalc command for B-Parking HLT path

```
brilcalc lumi --byls --normtag
/cvmfs/cms-bril.cern.ch/cms-lumi-pog/Normtags/normtag_PHYSICS.json
-i processedLumis.json --hltpath HLT_Mu9_IP6_part0_v* -o output.csv
```

Please note that we get luminosity for the specific BPH HLT path and save the output for pileupReCalc_HLTpaths.py

```
pileupReCalc_HLTpaths.py -i output.csv
--inputLumiJSON pileup_latest.txt -o My_HLT_corrected_PileupJSON.txt
--runperiod Run2
```

where, pileup_latest.txt is from

```
/afs/cern.ch/cms/CAF/CMSCOMM/COMM_DQM/certification/Collisions18/
13TeV/PileUp/pileup_latest.txt
```

Then, we substitute the usual pileup_latest.txt to My_HLT_corrected_PileupJSON.txt to obtain the PU distribution of data.

```
pileupCalc.py -i processedLumis.json
--inputLumiJSON My\_HLT\_corrected\_PileupJSON.txt
--calcMode true --minBiasXsec 69200 --maxPileupBin 120 --numPileupBins 120
MyDataPileupHistogram.root
```

With histograms above, one can create a PUWeight histogram distribution for an era's specific HLT path with commands below.

```
PUdata->Scale(1./PUdata->Integral(0,-1));
PUmc->Scale(1./PUmc->Integral(0,-1));
PUdata->Divide(PUmc);
```

Table A.1: Datasets used in the analysis

Data sample	Integrated Luminosity ($fb^{-}1$)
/ParkingBPH1/Run2018A-05May2019-v1/MINIAOD	0.866
/ParkingBPH2/Run2018A-05May2019-v1/MINIAOD	0.866
/ParkingBPH3/Run2018A-05May2019-v1/MINIAOD	0.866
/ParkingBPH4/Run2018A-05May2019-v1/MINIAOD	0.866
/ParkingBPH5/Run2018A-05May2019-v1/MINIAOD	0.866
/ParkingBPH6/Run2018A-05May2019-v1/MINIAOD	0.866
Total	5.20
/ParkingBPH1/Run2018B-05May2019-v2/MINIAOD	1.083
/ParkingBPH2/Run2018B-05May2019-v2/MINIAOD	1.083
/ParkingBPH3/Run2018B-05May2019-v2/MINIAOD	1.083
/ParkingBPH4/Run2018B-05May2019-v2/MINIAOD	1.083
/ParkingBPH5/Run2018B-05May2019-v2/MINIAOD	1.083
/ParkingBPH6/Run2018B-05May2019-v2/MINIAOD	1.083
Total	6.49
/ParkingBPH1/Run2018C-05May2019-v1/MINIAOD	1.079
/ParkingBPH2/Run2018C-05May2019-v1/MINIAOD	1.079
/ParkingBPH3/Run2018C-05May2019-v1/MINIAOD	1.079
/ParkingBPH4/Run2018C-05May2019-v1/MINIAOD	1.079
/ParkingBPH5/Run2018C-05May2019-v1/MINIAOD	1.079
Total	5.39
/ParkingBPH1/Run2018D-05May2019promptD-v1/MINIAOD	6.542
/ParkingBPH2/Run2018D-05May2019promptD-v1/MINIAOD	6.542
/ParkingBPH3/Run2018D-05May2019promptD-v1/MINIAOD	6.542
/ParkingBPH4/Run2018D-05May2019promptD-v1/MINIAOD	6.542
/ParkingBPH5/Run2018D-05May2019promptD-v1/MINIAOD	6.542
Total	32.7
ParkingBPH Total	50.78

A.2 Monte Carlo Samples

A.2.1 Signal Model and Simulation

The ggH production process (see Figure A.1) is generated at next-to-next-to-leading order (NNLO) and next-to-next-to-leading-log (NNLL) QCD and next-to-leading order (NLO) EW accuracies [64]. The Higgs boson mass is set to 125GeV for all signal samples. The cross sections, computed at NNLO+NNLL QCD and NLO EW accuracies and obtained from CERN Yellow Report 3, are 4.414 pb. The CMS detector response is modeled with GEANT4 [65].

Table ?? lists the signal Monte Carlo samples.

Figure A.1: Leading Feynman diagrams for ggH production mode

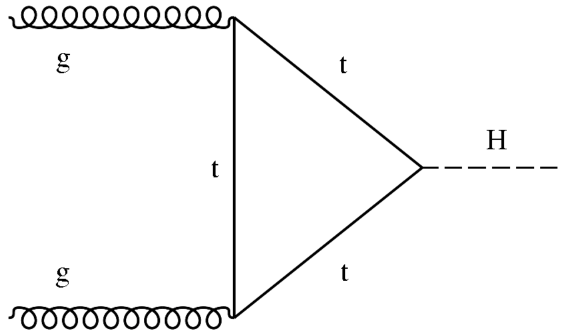

Sample
/ggH_HToSSTo4Tau_MH-125_TuneCP5_13TeV-powheg-pythia8/CAMPAIGN/MINIAODSIM
/ggH_HToSSTo4Tau_MH-125_MS-55_ctauS-1_TuneCP5_13TeV-powheg-pythia8/CAMPAIGN/MINIAODSIM
/ggH_HToSSTo4Tau_MH-125_MS-55_ctauS-10_TuneCP5_13TeV-powheg-pythia8/CAMPAIGN/MINIAODSIM
/ggH_HToSSTo4Tau_MH-125_MS-55_ctauS-100_TuneCP5_13TeV-powheg-pythia8/CAMPAIGN/MINIAODSIM
/ggH_HToSSTo4Tau_MH-125_MS-55_ctauS-1000_TuneCP5_13TeV-powheg-pythia8/CAMPAIGN/MINIAODSIM
/ggH_HToSSTo4Tau_MH-125_MS-40_ctauS-1_TuneCP5_13TeV-powheg-pythia8/CAMPAIGN/MINIAODSIM
/ggH_HToSSTo4Tau_MH-125_MS-40_ctauS-10_TuneCP5_13TeV-powheg-pythia8/CAMPAIGN/MINIAODSIM
/ggH_HToSSTo4Tau_MH-125_MS-40_ctauS-100_TuneCP5_13TeV-powheg-pythia8/CAMPAIGN/MINIAODSIM
/ggH_HToSSTo4Tau_MH-125_MS-40_ctauS-1000_TuneCP5_13TeV-powheg-pythia8/CAMPAIGN/MINIAODSIM
/ggH_HToSSTo4Tau_MH-125_MS-15_ctauS-1_TuneCP5_13TeV-powheg-pythia8/CAMPAIGN/MINIAODSIM
/ggH_HToSSTo4Tau_MH-125_MS-15_ctauS-10_TuneCP5_13TeV-powheg-pythia8/CAMPAIGN/MINIAODSIM
/ggH_HToSSTo4Tau_MH-125_MS-15_ctauS-100_TuneCP5_13TeV-powheg-pythia8/CAMPAIGN/MINIAODSIM
/ggH_HToSSTo4Tau_MH-125_MS-15_ctauS-1000_TuneCP5_13TeV-powheg-pythia8/CAMPAIGN/MINIAODSIM
/ggH_HToSSTo4Tau_MH-125_MS-7_ctauS-1_TuneCP5_13TeV-powheg-pythia8/CAMPAIGN/MINIAODSIM
/ggH_HToSSTo4Tau_MH-125_MS-7_ctauS-10_TuneCP5_13TeV-powheg-pythia8/CAMPAIGN/MINIAODSIM
/ggH_HToSSTo4Tau_MH-125_MS-7_ctauS-100_TuneCP5_13TeV-powheg-pythia8/CAMPAIGN/MINIAODSIM
/ggH_HToSSTo4Tau_MH-125_MS-7_ctauS-1000_TuneCP5_13TeV-powheg-pythia8/CAMPAIGN/MINIAODSIM

A.2.2 Background Monte Carlo

All samples were processed as recommended in the PPD Run2 Analysis Guideline [66]. Tables A.2-A.5 summarizes the background Monte Carlo used in this analysis.

a

Figure A.2: pt of the scalar products

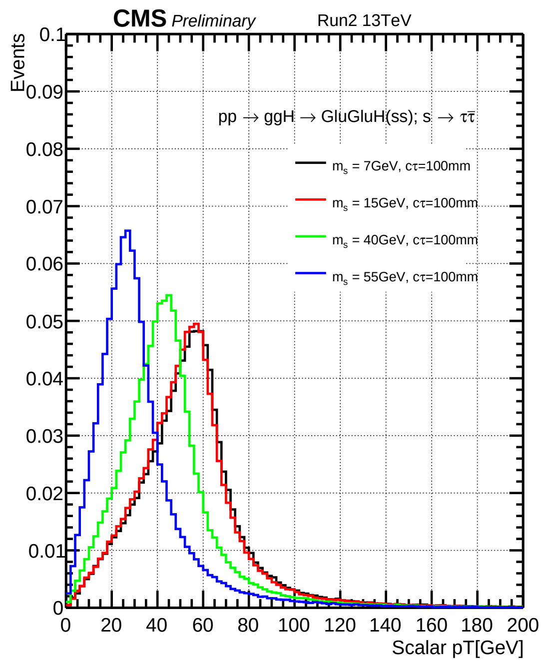

Figure A.3: DeltaR of the scalar products

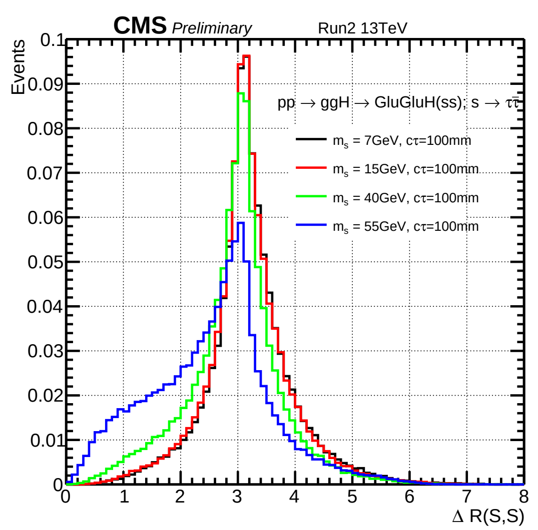

Figure A.4: liftime of the scalar products in the lab frame

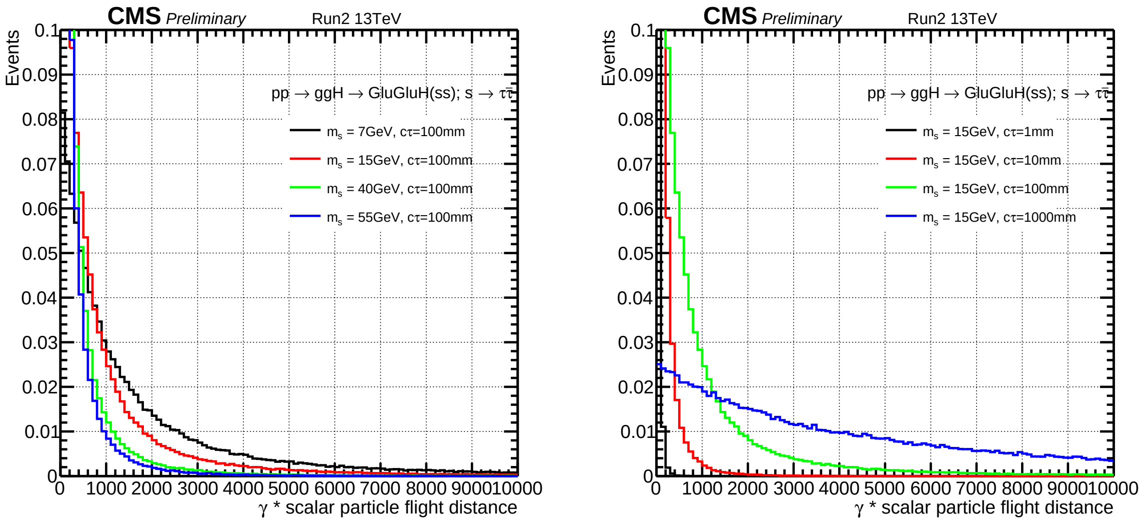

Table A.2: QCD MuEnriched Pt5 background Monte Carlo samples

Sample
/QCD_Pt-15to20_MuEnrichedPt5_TuneCP5_13TeV_pythia8/*-v3/MINIAODSIM
/QCD_Pt-20to30_MuEnrichedPt5_TuneCP5_13TeV_pythia8/*-v4/MINIAODSIM
/QCD_Pt-30to50_MuEnrichedPt5_TuneCP5_13TeV_pythia8/*-v3/MINIAODSIM
/QCD_Pt-50to80_MuEnrichedPt5_TuneCP5_13TeV_pythia8/*-v3/MINIAODSIM
/QCD_Pt-80to120_MuEnrichedPt5_TuneCP5_13TeV_pythia8/*_ext1-v2/MINIAODSIM
/QCD_Pt-120to170_MuEnrichedPt5_TuneCP5_13TeV_pythia8/*_ext1-v2/MINIAODSIM
/QCD_Pt-170to300_MuEnrichedPt5_TuneCP5_13TeV_pythia8/*-v3/MINIAODSIM
/QCD_Pt-300to470_MuEnrichedPt5_TuneCP5_13TeV_pythia8/*_ext3-v1/MINIAODSIM
/QCD_Pt-470to600_MuEnrichedPt5_TuneCP5_13TeV_pythia8/*_ext1-v2/MINIAODSIM
/QCD_Pt-600to800_MuEnrichedPt5_TuneCP5_13TeV_pythia8/*-v1/MINIAODSIM
/QCD_Pt-800to1000_MuEnrichedPt5_TuneCP5_13TeV_pythia8/*_ext3-v2/MINIAODSIM
/QCD_Pt-1000toInf_MuEnrichedPt5_TuneCP5_13TeV_pythia8/*-v1/MINIAODSIM

Table A.3: W,Z,H boson background Monte Carlo samples

Sample
/DYJetsToLL_M-50_TuneCP5_13TeV-madgraphMLM-pythia8/*-v1/MINIAODSIM
/WJetsToLNu_M-50_TuneCP5_13TeV-madgraphMLM-pythia8/*-v2/MINIAODSIM
/WW_M-50_TuneCP5_13TeV-madgraphMLM-pythia8/*-v2/MINIAODSIM
/WZ_M-50_TuneCP5_13TeV-madgraphMLM-pythia8/*-v3/MINIAODSIM
/ZZ_M-50_TuneCP5_13TeV-madgraphMLM-pythia8/*-v2/MINIAODSIM
/GluGluHToBB_M125_13TeV_amcatnloFXFX_pythia8/*-v1/MINIAODSIM

Table A.4: Top background Monte Carlo samples

Sample
/TTJets_TuneCP5_13TeV-madgraphMLM-pythia8/*-v1/MINIAODSIM
/ST_s-channel_4f_hadronicDecays_TuneCP5_13TeV-madgraph-pythia8/*_ext1-v1/MINIAODSIM
/ST_t-channel_top_5f_TuneCP5_13TeV-powheg-pythia8/*-v1/MINIAODSIM
/ST_t-channel_antitop_5f_TuneCP5_13TeV-powheg-pythia8/*-v1/MINIAODSIM
/ST_tW_antitop_5f_inclusiveDecays_TuneCP5_13TeV-powheg-pythia8/*_ext1-v1/MINIAODSIM
/ST_tW_top_5f_inclusiveDecays_TuneCP5_13TeV-powheg-pythia8/*_ext1-v1/MINIAODSIM

Table A.5: Monte Carlo sample summary

Sample
/QCD_Pt-15to20_MuEnrichedPt5_TuneCP5_13TeV_pythia8/*-v3/MINIAODSIM
/QCD_Pt-20to30_MuEnrichedPt5_TuneCP5_13TeV_pythia8/*-v4/MINIAODSIM
/QCD_Pt-30to50_MuEnrichedPt5_TuneCP5_13TeV_pythia8/*-v3/MINIAODSIM
/QCD_Pt-50to80_MuEnrichedPt5_TuneCP5_13TeV_pythia8/*-v3/MINIAODSIM
/QCD_Pt-80to120_MuEnrichedPt5_TuneCP5_13TeV_pythia8/*_ext1-v2/MINIAODSIM
/QCD_Pt-120to170_MuEnrichedPt5_TuneCP5_13TeV_pythia8/*_ext1-v2/MINIAODSIM
/QCD_Pt-170to300_MuEnrichedPt5_TuneCP5_13TeV_pythia8/*-v3/MINIAODSIM
/QCD_Pt-300to470_MuEnrichedPt5_TuneCP5_13TeV_pythia8/*_ext3-v1/MINIAODSIM
/QCD_Pt-470to600_MuEnrichedPt5_TuneCP5_13TeV_pythia8/*_ext1-v2/MINIAODSIM
/QCD_Pt-600to800_MuEnrichedPt5_TuneCP5_13TeV_pythia8/*-v1/MINIAODSIM
/QCD_Pt-800to1000_MuEnrichedPt5_TuneCP5_13TeV_pythia8/*_ext3-v2/MINIAODSIM
/QCD_Pt-1000toInf_MuEnrichedPt5_TuneCP5_13TeV_pythia8/*-v1/MINIAODSIM
/DYJetsToLL_M-50_TuneCP5_13TeV-madgraphMLM-pythia8/*-v1/MINIAODSIM
/WJetsToLNu_M-50_TuneCP5_13TeV-madgraphMLM-pythia8/*-v2/MINIAODSIM
/WW_M-50_TuneCP5_13TeV-madgraphMLM-pythia8/*-v2/MINIAODSIM
/WZ_M-50_TuneCP5_13TeV-madgraphMLM-pythia8/*-v3/MINIAODSIM
/ZZ_M-50_TuneCP5_13TeV-madgraphMLM-pythia8/*-v2/MINIAODSIM
/GluGluHToBB_M125_13TeV_amcatnloFXFX_pythia8/*-v1/MINIAODSIM
/TTJets_TuneCP5_13TeV-madgraphMLM-pythia8/*-v1/MINIAODSIM
/ST_s-channel_4f_hadronicDecays_TuneCP5_13TeV-madgraph-pythia8/*_ext1-v1/MINIAODSIM
/ST_t-channel_top_5f_TuneCP5_13TeV-powheg-pythia8/*-v1/MINIAODSIM
/ST_t-channel_antitop_5f_TuneCP5_13TeV-powheg-pythia8/*-v1/MINIAODSIM
/ST_tW_antitop_5f_inclusiveDecays_TuneCP5_13TeV-powheg-pythia8/*_ext1-v1/MINIAODSIM
/ST_tW_top_5f_inclusiveDecays_TuneCP5_13TeV-powheg-pythia8/*_ext1-v1/MINIAODSIM
/ggH_HToSSTo4Tau_MH-125_TuneCP5_13TeV-powheg-pythia8/*-v1/MINIAODSIM

APPENDIX B

OTHERS

REFERENCES

[1] S.Abachi et al. “Search for High Mass Top Quark Production in pp Collisions at s = 1.8 TeV.” In: *Phys. Lett.* 74 (1995), p. 12. DOI: 10.1103/PhysRevLett.74.2422. arXiv: 9411001 [hep-ex].

[2] F.Abe et al. “Observation of Top Quark Production in pp Collisions with the Collider Detector at Fermilab.” In: *Phys. Lett.* 74 (1995), p. 21. DOI: 10.1103/PhysRevLett.74.2626. arXiv: 9503002 [hep-ex].

[3] Serguei Chatrchyan et al. “Observation of a New Boson at a Mass of 125 GeV with the CMS Experiment at the LHC.” In: *Phys. Lett.* B716 (2012), pp. 30–61. DOI: 10.1016/j.physletb.2012.08.021. arXiv: 1207.7235 [hep-ex].

[4] Georges Aad et al. “Observation of a new particle in the search for the Standard Model Higgs boson with the ATLAS detector at the LHC.” In: *Phys. Lett.* B716 (2012), pp. 1–29. DOI: 10.1016/j.physletb.2012.08.020. arXiv: 1207.7214 [hep-ex].

[5] Y.Fukuda et al. “Evidence for Oscillation of Atmospheric Neutrinos.” In: *Phys. Lett.* 81 (1998), p. 9. DOI: 10.1103/PhysRevLett.81.1562. arXiv: 9807003 [hep-ex].

[6] Matthew Baumgart et al. “Non-Abelian Dark Sectors and Their Collider Signatures.” In: *JHEP* 04 (2009), p. 014. DOI: 10.1088/1126-6708/2009/04/014. arXiv: 0901.0283 [hep-ph].

[7] David E. Kaplan, Markus A. Luty, and Kathryn M. Zurek. “Asymmetric Dark Matter.” In: *Phys. Rev.* D79 (2009), p. 115016. DOI: 10.1103/PhysRevD.79.115016. arXiv: 0901.4117 [hep-ph].

[8] Yuk Fung Chan et al. “LHC Signatures of a Minimal Supersymmetric Hidden Valley.” In: *JHEP* 05 (2012), p. 155. DOI: 10.1007/JHEP05(2012)155. arXiv: 1112.2705 [hep-ph].

[9] Keith R. Dienes and Brooks Thomas. “Dynamical Dark Matter: I. Theoretical Overview.” In: *Phys. Rev.* D85 (2012), p. 083523. DOI: 10.1103/PhysRevD.85.083523. arXiv: 1106.4546 [hep-ph].

[10] Keith R. Dienes, Shufang Su, and Brooks Thomas. “Distinguishing Dynamical Dark Matter at the LHC.” In: *Phys. Rev.* D86 (2012), p. 054008. DOI: 10.1103/PhysRevD.86.054008. arXiv: 1204.4183 [hep-ph].

[11] Yanou Cui and Brian Shuve. “Probing Baryogenesis with Displaced Vertices at the LHC.” In: *JHEP* 02 (2015), p. 049. DOI: 10.1007/JHEP02(2015)049. arXiv: 1409.6729 [hep-ph].

[12] T Aaltonen et al. “High-precision measurement of the W boson mass with the CDF II detector.” In: *Science 376 (2022) 6589, 170-176* (2022). DOI: 10.1126/science.abk1781.

[13] Satoshi Mishima and Motoi Endo. "New physics interpretation of W-boson mass anomaly." In: (2022), p. 21. DOI: doi.org/10.48550/arXiv.2204.05965. arXiv: 2204.05965 [hep-ph].

[14] *CMS Supersymmetry Physics Results*. Tech. rep. Geneva: CERN, 2022. URL: https://twiki.cern.ch/twiki/bin/view/CMSPublic/PhysicsResultsSUS.

[15] Jared Barron and David Curtin. "On the Origin of Long-Lived Particles." In: *Journal of High Energy Physics* 61 (2020), p. 39. DOI: doi.org/10.48550/arXiv.2007.05538. arXiv: 2007.05538 [hep-ph].

[16] T. Aaltonen et al. "Search for heavy metastable particles decaying to jet pairs in $p\bar{p}$ collisions at $\sqrt{s} = 1.96$ TeV." In: *Phys. Rev.* D85 (2012), p. 012007. DOI: 10.1103/PhysRevD.85.012007. arXiv: 1109.3136 [hep-ex].

[17] V. M. Abazov et al. "Search for Resonant Pair Production of long-lived particles decaying to b anti-b in p anti-p collisions at s**(1/2) = 1.96-TeV." In: *Phys. Rev. Lett.* 103 (2009), p. 071801. DOI: 10.1103/PhysRevLett.103.071801. arXiv: 0906.1787 [hep-ex].

[18] Georges Aad et al. "Search for a light Higgs boson decaying to long-lived weakly-interacting particles in proton-proton collisions at $\sqrt{s} = 7$ TeV with the ATLAS detector." In: *Phys. Rev. Lett.* 108 (2012), p. 251801. DOI: 10.1103/PhysRevLett.108.251801. arXiv: 1203.1303 [hep-ex].

[19] Roel Aaij et al. "Search for long-lived particles decaying to jet pairs." In: *Eur. Phys. J.* C75.4 (2015), p. 152. DOI: 10.1140/epjc/s10052-015-3344-6. arXiv: 1412.3021 [hep-ex].

[20] Georges Aad et al. "Search for long-lived, weakly interacting particles that decay to displaced hadronic jets in proton-proton collisions at $\sqrt{s} = 8$ TeV with the ATLAS detector." In: *Phys. Rev.* D92.1 (2015), p. 012010. DOI: 10.1103/PhysRevD.92.012010. arXiv: 1504.03634 [hep-ex].

[21] Georges Aad et al. "Search for massive, long-lived particles using multitrack displaced vertices or displaced lepton pairs in pp collisions at $\sqrt{s} = 8$ TeV with the ATLAS detector." In: *Phys. Rev.* D92.7 (2015), p. 072004. DOI: 10.1103/PhysRevD.92.072004. arXiv: 1504.05162 [hep-ex].

[22] Khachatryan et al. "Search for long-lived neutral particles decaying to quark-antiquark pairs in proton-proton collisions at $\sqrt{s} = 8$ TeV." In: *Phys. Rev. D* 91 (1 Jan. 2015), p. 012007. DOI: 10.1103/PhysRevD.91.012007. URL: https://link.aps.org/doi/10.1103/PhysRevD.91.012007.

[23] Georges Aad et al. "Search for pair-produced long-lived neutral particles decaying in the ATLAS hadronic calorimeter in pp collisions at $\sqrt{s} = 8$ TeV." In: *Phys. Lett.* B743 (2015), pp. 15–34. DOI: 10.1016/j.physletb.2015.02.015. arXiv: 1501.04020 [hep-ex].

[24] R. Aaij et al. "Updated search for long-lived particles decaying to jet pairs." In: *Eur. Phys. J. C* 77.12 (2017), p. 812. DOI: 10.1140/epjc/s10052-017-5178-x. arXiv: 1705.07332 [hep-ex].

[25] Roel Aaij et al. "Search for massive long-lived particles decaying semileptonically in the LHCb detector." In: *Eur. Phys. J. C* 77.4 (2017), p. 224. DOI: 10.1140/epjc/s10052-017-4744-6. arXiv: 1612.00945 [hep-ex].

[26] Roel Aaij et al. "Search for long-lived heavy charged particles using a ring imaging Cherenkov technique at LHCb." In: *Eur. Phys. J. C* 75.12 (2015), p. 595. DOI: 10.1140/epjc/s10052-015-3809-7. arXiv: 1506.09173 [hep-ex].

[27] Albert M Sirunyan et al. "Search for new long-lived particles at $\sqrt{s} = 13$ TeV." In: *Phys. Lett.* B780 (2018), pp. 432–454. DOI: 10.1016/j.physletb.2018.03.019. arXiv: 1711.09120 [hep-ex].

[28] Albert M Sirunyan et al. "Search for long-lived particles with displaced vertices in multijet events in proton-proton collisions at $\sqrt{s}$ =13 TeV." In: *Phys. Rev. D* 98.9 (2018), p. 092011. DOI: 10.1103/PhysRevD.98.092011. arXiv: 1808.03078 [hep-ex].

[29] Albert M Sirunyan et al. "Search for long-lived particles decaying into displaced jets in proton-proton collisions at $\sqrt{s} = 13$ TeV." In: *Phys. Rev. D* 99.3 (2019), p. 032011. DOI: 10.1103/PhysRevD.99.032011. arXiv: 1811.07991 [hep-ex].

[30] Albert M Sirunyan et al. "Search for long-lived particles using nonprompt jets and missing transverse momentum with proton-proton collisions at $\sqrt{s} = 13$ TeV." In: *Phys. Lett. B* 797 (2019), p. 134876. DOI: 10.1016/j.physletb.2019.134876. arXiv: 1906.06441 [hep-ex].

[31] Albert M Sirunyan et al. "Search for new particles decaying to a jet and an emerging jet." In: *JHEP* 02 (2019), p. 179. DOI: 10.1007/JHEP02(2019)179. arXiv: 1810.10069 [hep-ex].

[32] *Search for long-lived particles decaying into displaced jets.* Tech. rep. CMS-PAS-EXO-19-021. Geneva: CERN, 2020. URL: https://cds.cern.ch/record/2717071.

[33] M. Aaboud et al. "Search for the Higgs boson produced in association with a vector boson and decaying into two spin-zero particles in the $H \to aa \to 4b$ channel in pp collisions at $\sqrt{s} = 13$ TeV with the ATLAS detector." In: *JHEP* 10 (2018), p. 031. DOI: 10.1007/JHEP10(2018)031. arXiv: 1806.07355 [hep-ex].

[34] Morad Aaboud et al. "Search for long-lived particles in final states with displaced dimuon vertices in pp collisions at $\sqrt{s} = 13$ TeV with the ATLAS detector." In: *Phys. Rev. D* 99.1 (2019), p. 012001. DOI: 10.1103/PhysRevD.99.012001. arXiv: 1808.03057 [hep-ex].

[35] Morad Aaboud et al. "Search for the Production of a Long-Lived Neutral Particle Decaying within the ATLAS Hadronic Calorimeter in Association with a Z Boson from pp Collisions at $\sqrt{s} = 13$ TeV." In: *Phys. Rev. Lett.* 122.15 (2019), p. 151801. DOI: 10.1103/PhysRevLett.122.151801. arXiv: 1811.02542 [hep-ex].

[36] Morad Aaboud et al. "Search for long-lived particles produced in pp collisions at $\sqrt{s} = 13$ TeV that decay into displaced hadronic jets in the ATLAS muon spectrometer." In: *Phys. Rev. D* 99.5 (2019), p. 052005. DOI: 10.1103/PhysRevD.99.052005. arXiv: 1811.07370 [hep-ex].

[37] Morad Aaboud et al. "Search for heavy long-lived multicharged particles in proton-proton collisions at $\sqrt{s} = 13$ TeV using the ATLAS detector." In: *Phys. Rev. D* 99.5 (2019), p. 052003. DOI: 10.1103/PhysRevD.99.052003. arXiv: 1812.03673 [hep-ex].

[38] Morad Aaboud et al. "Search for heavy charged long-lived particles in the ATLAS detector in 36.1 fb^{-1} of proton-proton collision data at $\sqrt{s} = 13$ TeV." In: *Phys. Rev. D* 99.9 (2019), p. 092007. DOI: 10.1103/PhysRevD.99.092007. arXiv: 1902.01636 [hep-ex].

[39] Morad Aaboud et al. "Search for long-lived neutral particles in pp collisions at $\sqrt{s} = 13$ TeV that decay into displaced hadronic jets in the ATLAS calorimeter." In: *Eur. Phys. J. C* 79.6 (2019), p. 481. DOI: 10.1140/epjc/s10052-019-6962-6. arXiv: 1902.03094 [hep-ex].

[40] Georges Aad et al. "Search for heavy neutral leptons in decays of W bosons produced in 13 TeV pp collisions using prompt and displaced signatures with the ATLAS detector." In: *JHEP* 10 (2019), p. 265. DOI: 10.1007/JHEP10(2019)265. arXiv: 1905.09787 [hep-ex].

[41] Georges Aad et al. "Search for Magnetic Monopoles and Stable High-Electric-Charge Objects in 13 Tev Proton-Proton Collisions with the ATLAS Detector." In: *Phys. Rev. Lett.* 124.3 (2020), p. 031802. DOI: 10.1103/PhysRevLett.124.031802. arXiv: 1905.10130 [hep-ex].

[42] Georges Aad et al. "Search for displaced vertices of oppositely charged leptons from decays of long-lived particles in pp collisions at $\sqrt{s}$ =13 TeV with the ATLAS detector." In: *Phys. Lett. B* 801 (2020), p. 135114. DOI: 10.1016/j.physletb.2019.135114. arXiv: 1907.10037 [hep-ex].

[43] Georges Aad et al. "Search for long-lived neutral particles produced in pp collisions at $\sqrt{s} = 13$ TeV decaying into displaced hadronic jets in the ATLAS inner detector and muon spectrometer." In: *Phys. Rev. D* 101.5 (2020), p. 052013. DOI: 10.1103/PhysRevD.101.052013. arXiv: 1911.12575 [hep-ex].

[44] Georges Aad et al. "Search for light long-lived neutral particles produced in pp collisions at $\sqrt{s} = 13$ TeV and decaying into collimated leptons or light hadrons with the ATLAS detector." In: *Eur. Phys. J. C* 80.5 (2020), p. 450. DOI: 10.1140/epjc/s10052-020-7997-4. arXiv: 1909.01246 [hep-ex].

[45] A.Tumeysan et al. "Search for long-lived particles produced in association with a Z boson in proton-proton collisions at s = 13 TeV." In: *JHEP.* (2021), p. 36. DOI: 10.1103/PhysRevLett.74.2422. arXiv: 2110.13218 [hep-ex].

[46] Brooks Thomas Shufang Su. "The LHC Discovery Potential of a Leptophilic Higgs." In: *Phys.Rev.D79:095014,2009* (2009), p. 25. DOI: 10.1103/PhysRevD.79.095014. arXiv: 0903.0667 [hep-ph].

[47] Z. Chacko, Hock-Seng Goh, and Roni Harnik. "The Twin Higgs: Natural electroweak breaking from mirror symmetry." In: *Phys. Rev. Lett.* 96 (2006), p. 231802. DOI: 10.1103/PhysRevLett.96.231802. arXiv: hep-ph/0506256 [hep-ph].

[48] Gustavo Burdman et al. "Folded supersymmetry and the LEP paradox." In: *JHEP* 02 (2007), p. 009. DOI: 10.1088/1126-6708/2007/02/009. arXiv: hep-ph/0609152 [hep-ph].

[49] Haiying Cai, Hsin-Chia Cheng, and John Terning. "A Quirky Little Higgs Model." In: *JHEP* 05 (2009), p. 045. DOI: 10.1088/1126-6708/2009/05/045. arXiv: 0812.0843 [hep-ph].

[50] Nathaniel Craig et al. "Naturalness in the Dark at the LHC." In: *JHEP* 07 (2015), p. 105. DOI: 10.1007/JHEP07(2015)105. arXiv: 1501.05310 [hep-ph].

[51] David Curtin and Christopher B. Verhaaren. "Discovering Uncolored Naturalness in Exotic Higgs Decays." In: *JHEP* 12 (2015), p. 072. DOI: 10.1007/JHEP12(2015)072. arXiv: 1506.06141 [hep-ph].

[52] Csaba Csaki et al. "Searching for displaced Higgs boson decays." In: *Phys. Rev.* D92.7 (2015), p. 073008. DOI: 10.1103/PhysRevD.92.073008. arXiv: 1508.01522 [hep-ph].

[53] *Facts and Figures about the LHC*. 2022. URL: https://home.cern/resources/faqs/facts-and-figures-about-lhc.

[54] *Facts and figures about the LHC*. URL: https://home.cern/resources/faqs/facts-and-figures-about-lhc.

[55] *Detector*. URL: https://cms.cern/detector.

[56] Scarlet Norberg et al. *Overview of CMS Physics Goals and Detector*. 2015. URL: https://twiki.cern.ch/twiki/bin/view/CMSPublic/WorkBookCMSExperiment.

[57] Alessandro Bartoloni et al. "The CMS ECAL barrel HV system." In: *Journal of Instrumentation* (2013). DOI: doi:10.1088/1748-0221/8/02/C02039.

[58] CMS Collaboration. "Calibration of the CMS hadron calorimeters using proton-proton collision data at $\sqrt{s} = 13$ TeV." In: *JINST 15* (2019). DOI: doi.org/10.1088/1748-0221/15/05/P05002.

[59] CMS Collaboration. "Alignment of the CMS silicon tracker during commissioning with cosmic rays." In: *JINST 5* (2010). DOI: 10.1088/1748-0221/5/03/T03009. arXiv:0910.2505: 1501.04020 (physics.ins-det).

[60] CMS collaboration. "Performance of reconstruction and identification of tau leptons in their decays to hadrons and tau neutrino in LHC Run-2." In: (2016).

[61] Khachatryan et al. *Muon POG – Muon Identification Run2*. 2020. URL: https://twiki.cern.ch/twiki/bin/viewauth/CMS/SWGuideMuonIdRun2.

[62] Matteo Cacciari, Gavin P. Salam, and Gregory Soyez. "The anti-k_t jet clustering algorithm." In: *JHEP* 04 (2008), p. 063. DOI: 10.1088/1126-6708/2008/04/063. arXiv: 0802.1189 [hep-ex].

[63] Khachatryan et al. *Jet Identification Run2 – 2018*. 2020. URL: https://twiki.cern.ch/twiki/bin/view/CMS/JetID13TeVRun2018.

[64] C. Mariotti Heinemeyer et al. "Handbook of LHC Higgs Cross Sections: 3. Higgs Properties." In: (2013), p. 404. DOI: 10.5170/CERN-2013-004. arXiv: 1307.1347 [hep-ph].

[65] S. Agostinelli et al. "GEANT4: A Simulation toolkit." In: *Nucl. Instrum. Meth. A* 506 (2003), pp. 250–303. DOI: 10.1016/S0168-9002(03)01368-8.

[66] Khachatryan et al. *Physics Performance Datasets – PPD Run2 Analysis Recipe Summary*. 2020. URL: https://twiki.cern.ch/twiki/bin/viewauth/CMS/PdmVAnalysisSummaryTable.

BIOGRAPHICAL SKETCH

The author was born, and then the author was "educated," at least to some degree. After finishing high school, the author completed a Bachelor of Science degree at Washington University in St.Louis. Following a decade in the work force in his discipline, the author went to FSU to pursue graduate work.